	2
Solid State Research	1972

Lincoln Laboratory

MASSACHUSETTS INSTITUTE OF TECHNOLOGY

LEXINGTON, MASSACHUSETTS

AD748836

2

Solid State Research

1972

Issued 30 August 1972

Lincoln Laboratory

MASSACHUSETTS INSTITUTE OF TECHNOLOGY

LEXINGTON, MASSACHUSETTS

ABSTRACT

This report covers in detail the solid state research work of the Solid
State Division at Lincoln Laboratory for the period 1 February through
30 April 1972. The topics covered are Solid State Device Research,
Quantum Electronics, Materials Research, Physics of Solids and Micro-
electronics. The Microsound work is sponsored by ABMDA and is re-
ported under that program.

CONTENTS

Contents

INTRODUCTION

I. SOLID STATE DEVICE RESEARCH

A new soft x-ray camera, which allows a 50X faster exposure of polymethyl methacrylate, has been developed for use in x-ray lithography. By using this camera, patterns with $0.6\,\mu m$ linewidths have been replicated with better than 0.2-μm resolution.

A technique has been developed which allows the fabrication of large-area masks for x-ray lithography. In this technique, 5-μm-thick windows are etched into 200-μm-thick silicon substrates which are used as frames to support the thin windows. The uniform 5-μm thickness is obtained by diffusing a heavily doped boron layer into the sample, and then etching from the reverse side with an etch that stops when the boron concentration reaches $\sim 2 \times 10^{19}/cm^3$.

Avalanche photodiodes have been made in InGaAs with Pt Schottky barriers and guard rings fabricated using proton bombardment. In reverse bias, these diodes have shown photocurrent multiplications of 200 times the low-bias response and rise times of <200 psec in response to a 1.06-μm mode-locked Nd:YAG laser. Reliability studies have been carried out on K_a-band GaAs IMPATT diodes fabricated using plated heat sinks of copper, silver or gold. These studies clearly indicate that plated silver heat sinks are superior to either gold or copper heat sinks. In addition, a comparison between devices made using proton-bombarded guard rings and devices made as inverted mesas showed that the proton-bombarded diodes had higher burnout resistance, with an average burnout temperature approximately 50°C higher than the inverted mesa diodes.

II. QUANTUM ELECTRONICS

Optical pumping of room temperature GaAs lasers has been carried out using a wavelength tunable, pulsed, optical parametric oscillator as the pump source. The dependence of laser operation on pump wavelength and power was studied for several GaAs samples. In these preliminary studies, conversion efficiencies of nearly 5 percent were obtained for high purity samples $(1.6 \times 10^{14}\,cm^{-3} \leqslant N_d + N_a \leqslant 1.6 \times 10^{16}\,cm^{-3})$. Si-doped samples having higher transparency in the vicinity of the band gap than the high purity samples showed broadband laser emission when pumped at shorter wavelengths.

Silicon-doped GaAs double heterostructure diodes have been fabricated. These devices have operated pulsed at room temperature. The observed lasing wavelength of $9400\,\mathring{A}$ corresponds to a transition involving a Si acceptor level that is shallower than those involved in spontaneous emission.

Studies of InAs lasers for pressure tuning in the 2.2 to 3.1-μm range have been undertaken. Pulsed operation, both with diodes and with optically pumped materials, is being examined. Band-to-band laser emission is observed in high purity, optically pumped material, while band-to-acceptor laser transitions are observed from diodes. Greater heating and thus

greater frequency chirping are seen in the optically pumped case. A faster, high repetition pulser is being constructed to reduce the chirp and to allow higher spectral resolution.

Continuous recombination radiation has been observed at temperatures between 2 and 20°K in InSb optically pumped by a CO laser. At $5.25\,\mu m$, 10 mW of CW radiation in a single axial mode was observed and, at $5.45\,\mu m$, lower power laser radiation was seen from a conduction-band-to-Zn-acceptor transition. Pulsed operation has also been achieved in a rod of InSb optically pumped by an array of GaAs diodes. Average power outputs of about 40 mW were observed at 10°K.

Studies of the tuning characteristics of a spin-flip Raman laser have been carried out using low density ($\sim 10^{15}\,cm^{-3}$) InSb. The observed tuning rate of $48 \pm 2\,MHz/G$ is three times larger than the previously observed rate for $10^{16}\,cm^{-3}$ material. At low carrier concentrations, the spontaneous linewidth should be narrower than for high concentration materials, reducing the influence of the cavity resonance condition and allowing the oscillation frequency to tune at a rate which is closer to that for spontaneous tuning (70 MHz/G). The absolute frequency of the spin-flip Raman laser was measured by the heterodyne technique, and short term frequency drifts of less than 2 MHz/sec were observed. Doppler limited spectroscopy of NO has also been carried out with this laser.

Pressure broadening has been studied for the very narrow line in the ν_2 band of H_2O which consists of two degenerate transitions, $16_{0,16} \leftarrow 15_{1,15}$ and $16_{1,16} \leftarrow 15_{0,15}$. The self-broadening coefficient of the full width was found to be 15 MHz/torr, while that for N_2 broadening was 0.6 MHz/torr. The observed ratio of 25:1 for these rates is in contrast to the 5:1 ratio reported for the 2.7-μm band.

III. MATERIALS RESEARCH

The optical absorption of n-type CdTe at room temperature has been measured between 0.9 and 12 μm for samples with carrier concentrations between 3.6×10^{16} and $1.8 \times 10^{18}\,cm^{-3}$. Intraband free-carrier absorption is the predominant absorption mechanism beyond 2 μm, but interband free-carrier absorption appears to be significant at shorter wavelengths.

The infrared-to-visible upconversion efficiency of $NaYF_4$:Yb, Er phosphors has been found to depend strongly on their degree of crystalline perfection. So far, the highest efficiencies have been obtained for samples prepared from NaF-rich melts, which crystallize directly in the low-temperature hexagonal form rather than undergoing a cubic-to-hexagonal transformation.

The compounds $MSbO_3$ (M = Li, Na, Rb or Ag) have been prepared in body-centered-cubic form by ion exchange between molten MNO_3 and $KSbO_3$, or $Tl\,bO_3$. The structures of $NaSbO_3$ and $AgSbO_3$ have been refined by analysis of x-ray diffraction data for single crystals obtained by the ion exchange technique.

The crystal structure of $CuTa_2O_6$ has been refined by x-ray diffraction analysis for a single crystal grown from a flux of excess CuO. The compound is a distorted perovskite in which each Cu atom has four coplanar nearest-neighbor anions and eight next-nearest-neighbor anions.

IV. PHYSICS OF SOLIDS

In the continuing phosphor upconversion program, several excitation sources, including a xenon arc lamp and a Nd-YAG laser, were employed to study the variation of visible emission as a function of infrared excitation in $NaY_{0.8}Yb_{0.18}Er_{0.02}F_4$. In our optical system, at an effective input intensity of $22\,W/cm^2$, a total radiant efficiency of over 5 percent was achieved and the efficiency was still rising at a significant rate with further increasing excitation. Since the above input intensity is well beyond what is presently available on a CW basis, it appears that saturation effects do not represent the primary limitation for this system.

The free energy model of a metal-insulator transition, formulated earlier for Ti_2O_3, is being extended to the case of V_2O_3. A theoretical study is under way, of the steady-state motion of an insulating phase pulse injected into a metallic phase film in the presence of an electric current.

Work in the high resolution laser spectroscopy programs continues. Zeeman tuning of several absorption lines of the paramagnetic NO gas was used to bring them into exact coincidence with fixed frequency CO laser lines and thereby obtain resolved absorption spectra of NO.

By using a $PbS_{0.82}Se_{0.18}$ diode laser operating at $4.7\,\mu m$, previous measurements on the molecule $C^{12}O^{16}$ were extended to the isotopic molecule $C^{13}O^{16}$. From a precise measurement of the spacing between absorption lines of these two molecules, the ratio of the reduced masses for the carbon isotopes was deduced and found to be in good agreement with the accepted mass spectrographic value.

The program of optically pumping molecular gas systems to produce sub-millimeter radiation has most recently turned to an investigation of population inversion from both the rotational and inversion-split states of NH_3. New stable transitions have been observed, identified and used as a source for studying the linewidth of hydrogenic donor transitions in high purity GaAs.

Samples of $Hg_{1-x}Cd_xTe$ with $x = 0.22$ and 0.31, cooled to below $25°K$, have been irradiated by 2.5-MeV electrons with dosages of up to $10^{15}/cm^2$. The samples were then annealed by heating for 15 minutes at progressively higher temperatures and returned to $8°K$ after each step to make measurements of conductivity, Hall coefficient, photoluminescence and photovoltaic response. The results appear to be interpretable in terms of the introduction by irradiation of energy levels in the forbidden gap.

In a theoretical study of imperfections in semiconductors, a model of the effect of lattice vacancies on the electrical properties of small-gap compound semiconductors has been formulated, based on T-matrix theory. The theory is being applied in particular to cases where the gap can be made to vanish by choice of composition or by the application of pressure.

V. MICROELECTRONICS

Considerable work has been required for equipment modifications and for equipment procurement to implement new processes or refinements in existing processes. The thin film

laboratory, in particular, has a large amount of materials processing which requires more efficient handling and scheduling to allow a continuation of short turnaround time for these tasks. Other areas of the microelectronics laboratory have also been active in equipment modifications and upgrading.

The environmental area has expanded its activity in life tests for the electron beam semi-conductor (EBS) units and GaAs microwave diodes, and has continued to evaluate all prototype hybrid integrated circuits and devices produced in the microelectronics facility.

The mask-making area has delivered approximately 400 masks since the first of the year, and the workload continues at a relatively high level. The inadequate environment of the present mask-making area continues to cause processing problems and limits the efforts to improve the throughput time.

A computer program to estimate the substrate area required for a particular circuit, based on its schematic, is nearly complete. Although the basic equation, which was derived empirically, has been employed for some time, the stored information on component size, substrate area, available package sizes and I/O pin configuration allows the computer to display the available options in package shape and size.

REPORTS ON SOLID STATE RESEARCH

15 February through 15 May 1972

PUBLISHED REPORTS

Journal Articles*

JA No.

3892	Shubnikov-de Haas Measurements in $Pb_{1-x}Sn_xSe$	J. Melngailis T.C. Harman W.C. Kernan	Phys. Rev. B 5, 2250 (1972), DDC AD-742593
3898	Persistent Photodielectric Lens Effect in Cadmium Sulfide	K.B. Kanarek[†] C.D. Wyche A.S. Pine	J. Appl. Phys. 43, 586 (1972), DDC AD-742595
3919	EuTe. I. Magnetic Behavior of Insulating and Conducting Single Crystals	N.F. Oliveira, Jr.[†] S. Foner[†] Y. Shapira[†] T.B. Reed	Phys. Rev. B 5, 2634 (1972), DDC AD-742603
3920	EuTe. ll. Resistivity and Hall Effect	Y. Shapira[†] S. Foner[†] N.F. Oliveira, Jr.[†] T.B. Reed	Phys. Rev. B 5, 2647 (1972), DDC AD-742606
3921	EuTe. lll. Ultrasonic Behavior	Y. Shapira[†] T.B. Reed	Phys. Rev. B 5, 2657 (1972), DDC AD-741613
3937	Fourier Expansion for Electronic Bands in Trigonal Tellurium and Selenium	G. Dresselhaus	Phys. Rev. B 5, 1538 (1972), DDC AD-738718
3939	Study of the Optical Shubnikov-de Haas Effect	F.P. Missell[†] M.S. Dresselhaus	Phys. Rev. B 5, 1364 (1972), DDC AD-738719
3943A	Non-Γ Donor Levels and Kinetics of Electron Transfer in n-Type CdTe	G.W. Iseler J.A. Kafalas A.J. Strauss H.F. MacMillan[†] R.H. Bube[†]	Solid State Commun. 10, 619 (1972)
3949	$Pb_{1-x}Sn_xTe$ Photovoltaic Diodes and Diode Lasers Produced by Proton Bombardment	J.P. Donnelly A.R. Calawa T.C. Harman A.G. Foyt W.T. Lindley	Solid-State Electron. 15, 403 (1972), DDC AD-742617

---

* Reprints available.

† Author not at Lincoln Laboratory.

Reports

JA No.

3953	Measurement of the Lattice Parameter of Wustite at High Temperatures	M. Hayakawa* J.B. Cohen* T.B. Reed	J. Am. Ceram. Soc. 55, 160 (1972)
3984	The Use of Lasers in Pollution Monitoring	I. Melngailis	IEEE Trans. Geosci. Electron. GE-10, 7 (1972), DDC AD-742624
3992	Preparation and Structure of a Pyrochlore and Perovskite in the $BiRhO_{3+x}$ System	J.M. Longo* P.M. Raccah* J.A. Kafalas J.W. Pierce	Mater. Res. Bull. 7, 137 (1972), DDC AD-738749
3995	p-n Junction Photodiodes in PbTe Prepared by Sb^+ Ion Implantation	J.P. Donnelly T.C. Harman A.G. Foyt W.T. Lindley	Appl. Phys. Letters 20, 279 (1972), DDC AD-744402
3996A	High Resolution Pattern Replication Using Soft X-Rays	D.L. Spears H.I. Smith	Electron. Letters 8, 102 (1972)

Meeting Speeches

MS No.

2621	Variations of Infrared Cyclotron Resonance and the Density of States Near the Conduction Band Edge of InSb	E.J. Johnson D.H. Dickey	Electronic Density of States, L.H. Bennett, ed. (NBS Special Publication 323, 1971), p.423
2628	On the Optical Properties and the Density of States in Arsenic	R.W. Brodersen* M.S. Dresselhaus	Electronic Density of States, L.H. Bennett, ed. (NBS Special Publication 323, 1971), p.39
2630	Optical Properties of Aluminum	G. Dresselhaus M.S. Dresselhaus D. Beaglehole*	Electronic Density of States, L.H. Bennett, ed. (NBS Special Publication 323, 1971), p.33
2631	Localized States in Narrow Band and Amorphous Semiconductors	D. Adler J. Feinleib	Electronic Density of States, L.H. Bennett, ed. (NBS Special Publication 323, 1971), p.493
2727	Theory of Antiferromagnetism and Ferrimagnetism	J.B. Goodenough	Chap. 24 in Physics of Electronic Ceramics, Part B, L.L. Hench and D.B. Dove, eds. (Marcel Dekker, Inc., New York, 1972), p.777
2906	Growth of Oxide Crystals	T.B. Reed	Ferrites: Proceedings of the International Conference, July 1970, Japan, Y. Hoshino, S. Iida and M. Sugimoto, eds. (University of Tokyo Press, Toyko, 1971), p.289

---

* Author not at Lincoln Laboratory.

MS No.

3075A	Brillouin Spectroscopy in Cadmium Sulfide: Acoustoelectric and Anharmonic Effects and Resonance Scattering	A.S. Pine	Proceedings of the Second International Conference on Light Scattering in Solids, Paris, 19-23 July 1971, M. Balkanski, ed. (Flammarion Sciences, Paris, 1971), p. 46
3076	Raman Scattering in Tellurium	A.S. Pine G. Dresselhaus	Proceedings of the Second International Conference on Light Scattering in Solids, Paris, 19-23 July 1971, M. Balkanski, ed. (Flammarion Sciences, Paris, 1971), p. 26.
3129	Molecular and Lattice Vibrations in Solid Ammonia	A.S. Pine C.J. Glassbrenner G. Dresselhaus	Proceedings of the International Conference on Phonons, Rennes, France, 26-28 July 1971 (Flammarion Sciences, Paris, 1971), p. 258
3153	Preparation and Properties of $Pb_{1-x}Cd_xS$	A.R. Calawa J.A. Mroczkowski T.C. Harman	J. Electron. Mater. No. 1, 191 (1972)

* * * * *

UNPUBLISHED REPORTS

Journal Articles

JA No.

3905	Structure of Orthorhombic $V_{0.95}Cr_{0.05}O_2$	J.W. Pierce J.B. Goodenough	Accepted by Phys. Rev. B
3942A	Observation of Λ-Doubling and Zeeman Splitting in the Fundamental Absorption Band of Nitric Oxide	K.W. Nill F.A. Blum A.R. Calawa T.C. Harman	Accepted by Chem. Phys. Letters
3970	Observation of Nuclear Hyperfine Splitting in the Infrared Vibration-Rotation Absorption Spectrum of the NO Molecule	F.A. Blum K.W. Nill A.R. Calawa T.C. Harman	Accepted by Chem. Phys. Letters
3974	Amplitude Renormalization Factor in Two-Magnon Raman Scattering	R.W. Davies	Accepted by Phys. Rev. B
3985	Tunable Lasers and Their Applications	H.R. Schlossberg* P.L. Kelley	Accepted by Physics Today

---

* Author not at Lincoln Laboratory.

Reports

JA No.

4001	X-Ray Lithography: A New High Resolution Replication Process	D. L. Spears H. l. Smith	Accepted by Solid State Technology
4006	Tunable Laser Spectroscopy of the ν_1 Band of SO_2	E. D. Hinkley A. R. Calawa P. L. Kelley S. A. Clough*	Accepted by J. Appl. Phys.
4015	Measurement of the Gain Line-shape of a Gas Laser Using a Tunable Semiconductor Laser	F. A. Blum K. W. Nill A. R. Calawa T. C. Harman	Accepted by Appl. Phys. Letters
4028	A Laser Scanner for Integrated Circuit Testing	R. E. McMahon	Accepted by Proc. lEEE
MS-3175	Valence-Bond Approach to Magnetic Semiconductors	J. B. Goodenough	Accepted by New Developments in Semiconductors (Wolters-Noordhoff, Gronigen)

Meeting Speeches†

MS No.

2951G	Localized vs Itinerant Electrons in Transition-Metal Monoxides	J. B. Goodenough	Colloquia in Solid State Science, Arizona State University, Tempe, Arizona, 12-14 April 1972
3043E	Semiconductor-to-Metal Transitions	J. B. Goodenough	
3356	Perovskite Polytypes	J. B. Goodenough	
2989E	A Laser Scanner for Integrated Circuit Testing	R. E. McMahon	lEEE 1972 Reliability Physics Symposium, Las Vegas, Nevada, 5-7 April 1972
3155A	The Use of Lasers in Pollution Monitoring	l. Melngailis	Third Latvian Conference on Technical Sciences, York University, Toronto, Ontario, 12-14 May 1972
3192A	Recent Developments in Tunable Infrared Lasers	A. Mooradian	Seminar, Naval Research Laboratory, Washington, D.C., 6 April 1972
3245	X-Ray Replication of Scanning Electron Microscope Generated Patterns	D. L. Spears H. l. Smith E. Stern	5th International Conference of Electron and Ion Beam Society, Houston, Texas, 7-12 May 1972

* Author not at Lincoln Laboratory.

† Titles of Meeting Speeches are listed for information only. No copies are available for distribution.

MS No.

3249	Resistivity of $Pb_{1-x}Sn_xSe$ vs Hydrostatic Pressure	J. Melngailis T. C. Harman J. A. Kafalas	
3254	Free-Carrier Absorption in n-Type PbTe	A. J. Strauss	
3296	$PbS_{1-x}Se_x$ Tunable Lasers for High Resolution Infrared Spectroscopy	K. W. Nill F. A. Blum A. R. Calawa T. C. Harman	Conference on the Physics of IV-VI Compounds and Alloys, Moore School of Electrical Engineering, University of Pennsylvania, Philadelphia, 24-25 March 1972
3307A	PbTe Photodiodes Fabricated by Sb^+ Ion Implantation	J. P. Donnelly T. C. Harman A. G. Foyt W. T. Lindley	
3322	Control of Imperfections in Crystals of $Pb_{1-x}Sn_xTe$, $Pb_{1-x}Sn_xSe$, and $PbS_{1-x}Se_x$	T. C. Harman	
3255	Flexible, Beam-Leaded Substrates Utilizing Aluminum Interconnections and Beam Leads	F. J. Bachner	The American Ceramic Society, Inc., 74th Annual Meeting and Exposition, Washington, D.C., 6-11 May 1972
3275	Measurement of the Frequency Gain Profile of a CO Laser Using a Tunable Semiconductor Laser	F. A. Blum K. W. Nill A. R. Calawa T. C. Harman	
3276	High Resolution Infrared Spectroscopy of NO Using a Tunable PbSSe Laser	K. W. Nill F. A. Blum A. R. Calawa T. C. Harman	
3277	Tunable Laser Spectroscopy of the ν_1 Band of SO_2	P. L. Kelley E. D. Hinkley A. R. Calawa S. A. Clough*	VII International Quantum Electronics Conference, Montreal, Canada, 8-11 May 1972
3337	Tunable Semiconductor Lasers	A. Mooradian	
3362	Submillimeter Lasers Optically Pumped Off Resonance	H. R. Fetterman H. R. Schlossberg* J. Waldman C. D. Parker P. E. Tannenwald	

---

* Author not at Lincoln Laboratory.

Reports

---

* Author not at Lincoln Laboratory.

MS No.

3307	PbTe Photodiodes Fabricated by Sb^+ Ion Implantation	J. P. Donnelly T. C. Harman A. G. Foyt W. T. Lindley	
3308	InSb p–n Junction Photodiodes Fabricated by Zn^+ Ion Implantation	A. G. Foyt C. E. Hurwitz J. P. Donnelly W. T. Lindley	1972 IRIS Detector Specialty Group Meeting, Orlando, Florida, 15–17 March 1972
3309	Guarded Planar InSb n–p Photo-diodes Fabricated by Proton Bombardment	C. E. Hurwitz F. J. Leonberger A. G. Foyt W. T. Lindley J. P. Donnelly	
3318	High Resolution Infrared Spec-troscopy Using Tunable Semi-conductor Lasers	K. W. Nill	Physics Colloquium, Ohio State University, 15 February 1972
3357	Semiconductor Lasers for Spec-troscopy and Pollution Monitoring	I. Melngailis	IEEE Electron Devices Meeting Raytheon Company, Bedford, Massachusetts, 13 April 1972
3358	Nonlinear Optics	P. L. Kelley	American Physical Society Meeting, Poughkeepsie, New York, 21–22 April 1972

ORGANIZATION

SOLID STATE DIVISION

A. L. McWhorter, *Head*
P. E. Tannenwald, *Associate Head*
C. R. Grant, *Assistant*

QUANTUM ELECTRONICS

A. Mooradian, *Leader*
P. L. Kelley, *Associate Leader*

Brueck, S. R. J.	Heckscher, H.
Burke, J. W.	Johnson, E. J.
Chinn, S. R.	Moulton, P. F.*
Eng, R. S.	Pine, A. S.
Hancock, R. C.	Rossi, J. A.

ELECTRONIC MATERIALS

J. B. Goodenough, *Leader*
A. J. Strauss, *Associate Leader*

Anderson, C. H., Jr.	LaFleur, W. J.
Batson, D. A.	Lavine, M. C.†
Button, M. J.	Mastromattei, E. L.
Coppola, A. J.	Mikkelsen, J. C.,
Delaney, E. J.	Mroczkowski, I. H.
Fahey, R. E.	Owens, E. B.
Fan, J. C. C.	Pantano, J. V.
Finn, M. C.	Pierce, J. W.
Hong, H. Y-P	Plonko, M. C.
Hsieh, J. J.	Reed, T. B.
Iseler, G. W.	Tracy, D. M.
Kafalns, J. A.	Zavracky, P. M.

MICROELECTRONICS

R. E. McMahon, *Leader*

Bachner, F. J.	Gray, R. V.
Beatrice, P. A.	McGonagle, W. H.
Clough, T. F.	Mountain, R. W.
Cohen, R. A.	Pichler, H. H.
Durant, G. L.	Smythe, D. L.
Grant, L. L.	Wilde, R. E.

SOLID STATE PHYSICS

J. G. Mavroides, *Co-Leader*
H. J. Zeiger, *Co-Leader*
G. B. Wright, *Assistant Leader* (LOA)

Allen, J. W.	Henrich, V. E.
Barch, W. E.	Johnson, L.*
Blum, F. A., Jr.	Kernan, W. C.
Brodersen, R. W.*	Kolesar, D. F.
Davies, R. W.	Korn, D. M.
DeFeo, W. E.	Larsen, D. M.
Dresselhaus, G. F.	Melngailis, J.
Dwight, K., Jr.	Menyuk, N.
Feldman, B.	Nill, K. W.
Fetterman, H.	Parker, C. D.
Groves, S. H.	Seccombe, D.*

APPLIED PHYSICS

I. Melngailis, *Leader*
A. G. Foyt, *Assistant Leader*
T. C. Harman, *Assistant Leader*

Belanger, L. J.	McBride, W. F.
Calawa, A. R.	Murphy, R. A.
Carter, F. B.	Orphanos, W. G.
DeMeo, N.	Paladino, A. E.
Donnelly, J. P.	Ralston, R. W.
Ferrante, G. A.	Spears, D. L.
Hurwitz, C. E.	Stillman, G. E.
Krohn, L., Jr.	Ward, J. H. R., III
Leonberger, F. F.*	Wolfe, C. M.
Lincoln, G. A., Jr.	Youtz, P.
Lindley, W. T.	

MICROSOUND

E. Stern, *Leader*

Alusow, J. A.	Smith, H. I.
Brogan, W. T.	Smith, J. A.
Burke, B. E.	Williamson, R. C.
Kalish, D.	

---

* Research Assistant

† Part Time

xviii

I. SOLID STATE DEVICE RESEARCH

A. SOFT X-RAY LITHOGRAPHIC EXPOSURE APPARATUS

Soft x-ray lithographic exposure apparatus has been built which allows a 5-cm^2 area of polymethyl methacrylate resist to be adequately exposed in less than 30 minutes, and the same area of Kodak Micro-Negative resist, in less than 8 minutes. This represents a factor-of-50 reduction over the exposure times previously reported.[1,2] The apparatus, shown in Fig. 1-1, incorporates an electron beam evaporation gun[3] with the target material firmly attached to the hearth for efficient heat dissipation. A 2-cm-diameter filament is shielded from the target (here aluminum), which greatly reduces the build-up of soft x-ray absorbing tungsten on it. Characteristic 8.3-Å Al$_{K\alpha}$ x-rays emanate from the 1-mm-diameter focal spot and pass through a 0.1-mil aluminum filter, which absorbs the thermal radiation and any stray electrons, yet passes 80 percent of the x-rays. The polymer-resist coated wafer with an x-ray mask clamped on it is located 32 mm from the target. The water-cooled camera is attached to a vacuum blank-off plate. During operation, 50 cc/min of water flow is sufficient to keep the wafer near room temperature.
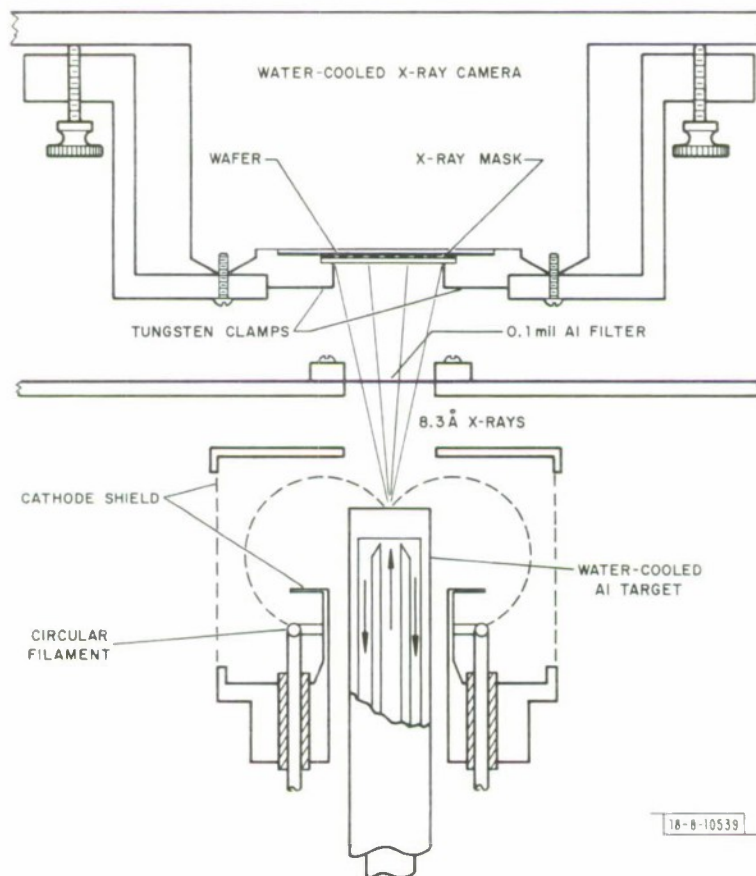

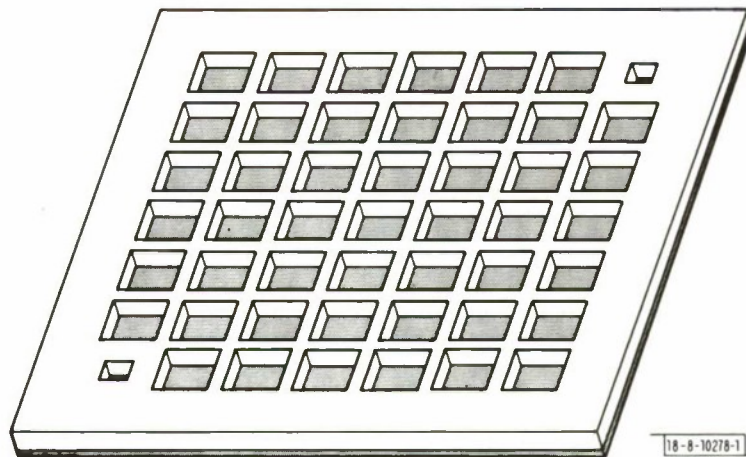Fig. 1-1. Diagram of soft x-ray exposure apparatus.

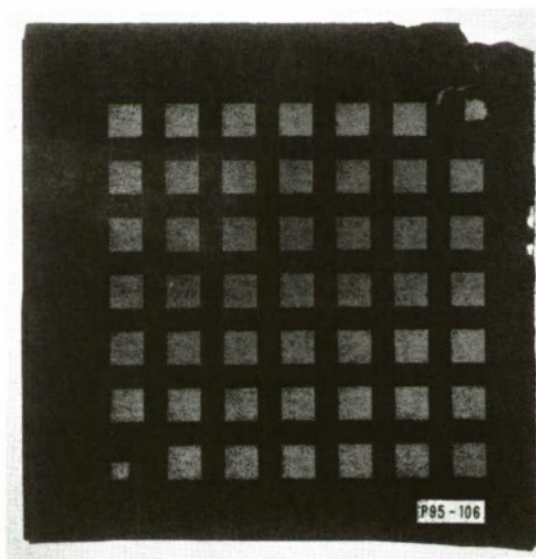Fig. I-2(a). Proposed structure for a large area soft x-ray mask substrate.

Fig. I-2(b). Photograph of a one-inch-square silicon wafer with an array of 5-μm-thick, 60-mil-square membranes etched into it.

Under normal operating conditions (8 kV and 50 mA of electron beam current), the surface of the aluminum target is molten in the 1-mm focal spot and evaporates at a very low rate. This evaporation keeps the aluminum surface free of contamination, but requires changing the 0.1-mil filter after every 20 to 50 hours of use.

Interdigital surface wave transducer patterns with 0.6-μm linewidths have been replicated in this system with better than 0.2-μm resolution. With a copper target, it should be possible to obtain 500-Å resolution at the expense of a somewhat longer exposure time.

D. L. Spears

B. SUBSTRATE FOR SOFT X-RAY MASK

The substrate of a soft x-ray lithographic mask, which provides the support for the absorbent gold film in which the device pattern exists, must be smooth, flat and transparent to soft x-rays.[1] Due to the strong absorption coefficient of all solid materials in the 10-Å wavelength region ($\gtrsim$1000 cm^{-1}), this substrate must be extremely thin, a few microns, and it requires an adequate support frame. A 1-cm^2 active area mask could be fabricated on a structure, such as that shown in Fig. I-2(a), which consists of a window lattice frame with a thin membrane attached across the bottom surface. On each window opening, a set of submicron device patterns could be placed. It is desirable that the lattice frame and the membrane be made of the same material to avoid differential thermal expansion, which would severely degrade ultra-high resolution pattern replication.

Such substrates have been made from silicon, which has a relatively low absorption coefficient in the 7- to 15-Å region. A standard 8-mil-thick silicon wafer diffused with boron provides the starting material. The boron layer serves two purposes. First, it renders the silicon inert to the etching action of the ethylene diamine-pyrocatechol-water chemical etch,[4] enabling thin membranes of precise thickness to be made. Second, the addition of boron contracts the silicon lattice (due to the small covalent radius of boron) resulting in membranes which are under tension and thus very flat. Figure I-2(b) is a transmission photograph of a one-inch-square silicon wafer in which an array of 60-mil-square, 5-μm-thick membranes were etched. The pattern was defined on the back of the wafer in a 2000-Å layer of SiO$_2$, which is not attacked by the etch. The etch was carried out at 115°C in a reflux boiler. The optical semi-transparency of silicon a few microns thick allows us to visually determine the uniformity of the membrane, which is generally better than 0.1 μm.

The etch is strongly anisotropic, etching 16 times faster into the $\langle 100 \rangle$ plane than the $\langle 111 \rangle$ plane.[5] Thus, a square opening in the SiO$_2$ etches a hole in $\langle 100 \rangle$ silicon the shape of a perfect truncated pyramid with sides of $\langle 111 \rangle$ planes. The tapered edges allow full use of the window area. In addition, this structure is easily handled. It can be immersed and agitated in cleaning solutions and blown dry with an air brush without damage. Three different boron diffusions were carried out using a boron nitride source under approximate complementary error function conditions, which gave etched membranes 5.0, 3.3 and 2.4 μm thick. The concentration of boron at the critical depth for these wafers is calculated to be about 2×10^{19} cm^{-3}, which is somewhat less than that reported in Ref. 4.

D. L. Spears
R. A. Cohen

3

C. HIGH-SPEED InGaAs AVALANCHE PHOTODIODES

Avalanche photodiodes which have gains of more than 200 at subnanosecond response times have been fabricated in InGaAs alloys.

The structure used for these devices consists of a semi-transparent Pt Schottky barrier on an epitaxial layer of InGaAs, as shown in Fig. I-3. 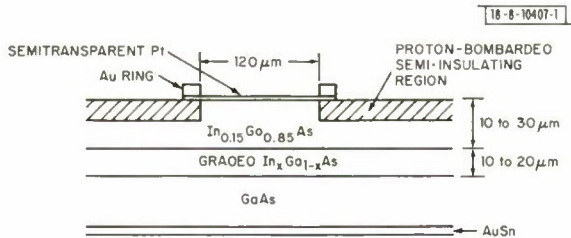The material is prepared by vapor-phase epitaxy. A graded layer of InGaAs is first grown on an n^+ GaAs substrate followed by a constant composition InGaAs layer which forms the active part of the device. Edge breakdown at the perimeter of the Schottky barrier is effectively eliminated by a high resistivity layer, about $4\,\mu m$ deep, created by proton bombardment. The proton bombardment also provides surface passivation.

Fig. I-3. Cross-section of an InGaAs avalanche photodiode fabricated with a platinum Schottky barrier and a proton-bombarded guard ring.

A mode-locked, Nd-doped YAG laser emitting at $1.06\,\mu m$ was used to evaluate the speed of response of these devices. The output pulse shown in Fig. I-4 was measured across the 50-ohm load of a sampling oscilloscope with a device operating at a gain of approximately 200 and a bias voltage of $-35.0\,V$. Higher avalanche gains with this same speed of response have been observed, but it is difficult to accurately determine their value. This is due to the small value of the primary photocurrent at low bias and at incident power levels low enough to avoid gain saturation at operating bias (maximum gain). The rise and fall time observed is less than 200 psec, although it is not clear at this time whether this is limited by the response speed of the detector or by the output pulse of the laser. Using a spectrum analyzer, the response of the diode has been observed to be essentially flat out to more than 1.9 GHz at this gain.

The ultimate objective of this work is to develop a $1.06-\mu m$ avalanche photodiode with a quantum efficiency greater than 30 percent (at $1.06\,\mu m$), a gain of more than 100, and an equivalent noise current less than 3 mA (corresponding to the noise figure of the first stage amplifier) for use in a high data rate (1 Gbps) satellite communication system. The desired rise and fall time of this detector is <100 psec. However, the 1.9-GHz response time observed with the
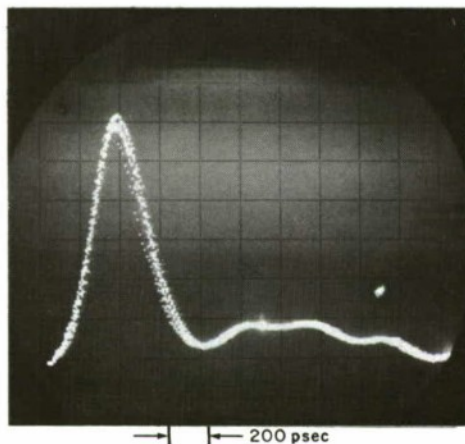

Fig. I-4. Photocurrent response of an InGaAs avalanche diode to $1.06-\mu m$ pulses from a mode-locked Nd:YAG laser. The response shown is for a diode avalanche gain of 200 times the low bias response.

4

5-mil-diameter devices is adequate for a 1-Gbps data rate system. An equivalent noise current of about 2 mA for the operating gain of ~200 has been measured at 30 MHz. The required gain has already been achieved, but not with the desired quantum efficiency at 1.06 µm. The spectral response of an $In_{0.15}Ga_{0.85}As$ detector shown in Fig. I-5 has a long wavelength cutoff at 1.03 µm
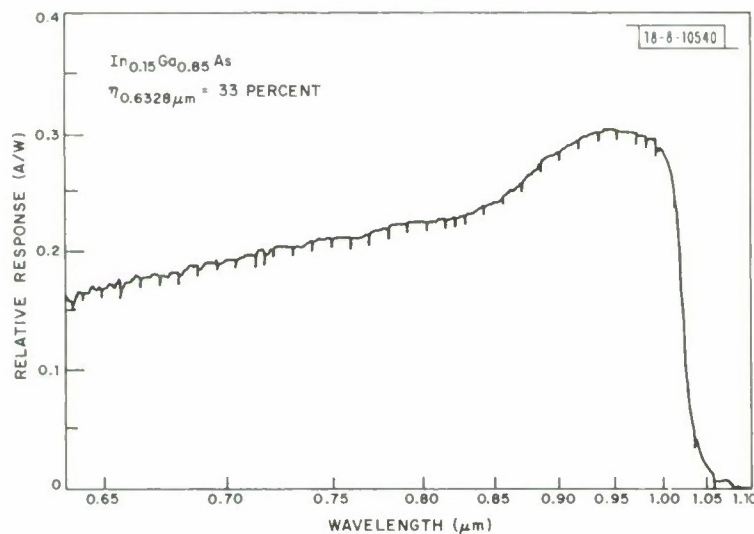

Fig. I-5. Relative spectral response of an $In_{0.15}Ga_{0.85}As$ photodiode, at low bias, as a function of wavelength.

and the quantum efficiency at 1.06 µm is low. However, the peak quantum efficiency at 0.95 µm is about 32 percent, and values from 40 to 60 percent, depending on the thickness of the Pt Schottky barrier, are routinely obtained. From these results, we conclude that the attainment of high quantum efficiency at 1.06 µm requires material with about 20-percent InAs. Devices are currently being fabricated with material of this composition.

G. E. Stillman   W. T. Lindley
C. M. Wolfe   P. Moulton
A. G. Foyt   I. Melngailis

D. PROTON GUARDED GaAs IMPATT DIODES AT K_a BAND

In this section, the fabrication of the K_a-band GaAs IMPATT diodes mentioned in the previous Solid State Research Report[6] is presented in detail. In addition, the results of reliability and life test experiments are described. These experiments show that silver-plated heat sinks are superior to either gold or copper heat sinks, and also that diodes made using proton guarding have a burn-out resistance superior to those made in the inverted mesa configuration.

Both bulk samples and n-n$^+$ epitaxial layers have been used as substrates. The first several steps of the fabrication procedure of a bulk material, Schottky-barrier device are shown in Fig. I-6. After the GaAs surface is cleaned and free-etched, a grid of 3.5-µm-deep channels is etched into the face of the sample using SiO_2 as an etch mask. The SiO_2 is then removed and platinum is plated over the entire surface of the sample, forming the active Schottky-barrier junction. A thick layer of silver, followed by a thin layer of gold for mounting purposes, is then plated on the platinum. The choice of silver as the heat sink material was made on the basis of an
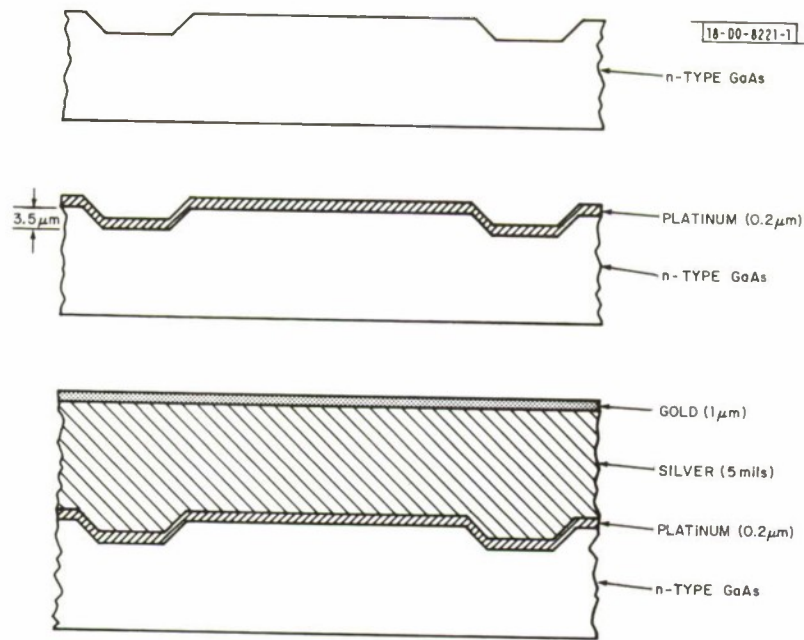
5

18-DO-8221-1

n-TYPE GaAs

3.5 μm

PLATINUM (0.2 μm)

n-TYPE GaAs

GOLD (1 μm)

SILVER (5 mils)

PLATINUM (0.2 μm)

n-TYPE GaAs

Fig. I-6. Fabricatian sequence far the K_a-band GaAs IMPATT diode (side 1).

18-DO-8222-1

n-TYPE GaAs (3 μm)

PLATINUM (0.2 μm)

SILVER (5 mils)

GOLD (1 μm)

HIGH-RESISTIVITY PROTON-GUARDED GaAs

GOLD (3.5 μm)

PLATINUM (0.2 μm)

CHROMIUM (0.04 μm)

n-TYPE GaAs

PLATINUM (0.2 μm)

SILVER (5 mils)

GOLD (1 μm)

Fig. I-7. Fabricatian sequence far the K_a-band GaAs IMPATT diode (side 2).

6

experiment designed to compare the operating life of devices with gold, silver and copper heat sinks. In this experiment, a number of device-like structures with each of the metalization schemes were biased into avalanche breakdown, at power levels just below the burn-out point, and the time taken for each to fail was monitored. Although the current number of failures is small, it is clear that the lifetime of the GaAs-Pt-Ag metalization is considerably longer than that of either the copper or gold metalizations.

The plated wafer is then mounted on a sapphire slab and the GaAs is mechanically and chemically removed until the grid of channels just appears over the entire back face, as depicted in Fig. I-7. Thus, the thickness of the GaAs is reduced to less than the channel depth, 3.5 μm. A chrome (400 Å), platinum (2000 Å) and gold (5000 Å) layer is then sputtered onto the back side of the GaAs; an additional 3-μm-layer of gold is plated onto the sputtered gold, and a contact pattern is defined on the back surface photolithographically. The gold, platinum and chrome are then etched away from the unmasked areas delineating the contact, as shown in the figure. It should be noted that the contact is not ohmic, but will in operation be a forward-biased Schottky barrier. Although some ohmic contacting schemes have been tried, using Au-Ge alloys, the performance of devices with Schottky-barrier back contacts has thus far been superior.
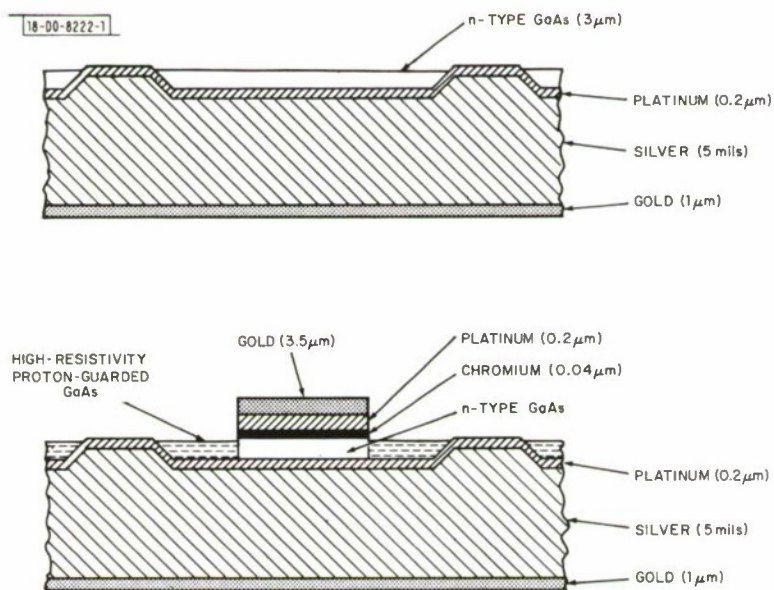
The device is then bombarded with 400-keV protons. The protons do not penetrate the 3.5-μm Au contacts, but are capable of penetrating 4 μm of GaAs. The effect of the protons is to convert the entire layer of GaAs surrounding the back contacts into semi-insulating material. This process serves to delineate the active device area and also to suppress edge breakdown.

A sketch of the finished device is shown in Fig. I-8. Although the proton guarding technique has other advantages, the convenience of the technique can be appreciated at this point. The optimum device diameter at these frequencies is approximately 2 mils, rendering conventional etched-mesa techniques difficult. In the present scheme, the accuracy with which the devices can be delineated is limited only by the accuracy with which the bombardment mask, the back contact, can be defined. It is also apparent that no increased difficulty attaches to the creation of arbitrarily shaped devices by this method, e.g., ring structures.

After the proton guarding operation, the devices are separated with a multi-wire string saw. Each device is then soldered onto a gold-

Fig. I-8. Cross-section sketch of the K_a-band GaAs IMPATT diode.

plated, threaded copper cylinder using a Au-Sn solder and contacted using thermal-compression bonding with a 3- by 0.5-mil gold ribbon which extends from an alumina stand-off. A photograph of a mounted and contacted device is shown in Fig. I-9.

These basic fabrication steps have been adapted to produce a variety of different IMPATT diodes. The essential features of these configurations are shown and compared in Fig. I-10. The p-n junction devices were fabricated by the implantation of zinc ions into bulk n-type material. Microwave results on these samples are entirely comparable to those from Schottky-barrier diodes on the same material. As mentioned before, epitaxial material has also been used with no measurable improvement in the microwave results.

Fig.1-9. Photograph of a K_a-bond GaAs IMPATT diode mounted on a copper heat sink and contacted with a 0.5 × 3-mil gold ribbon.
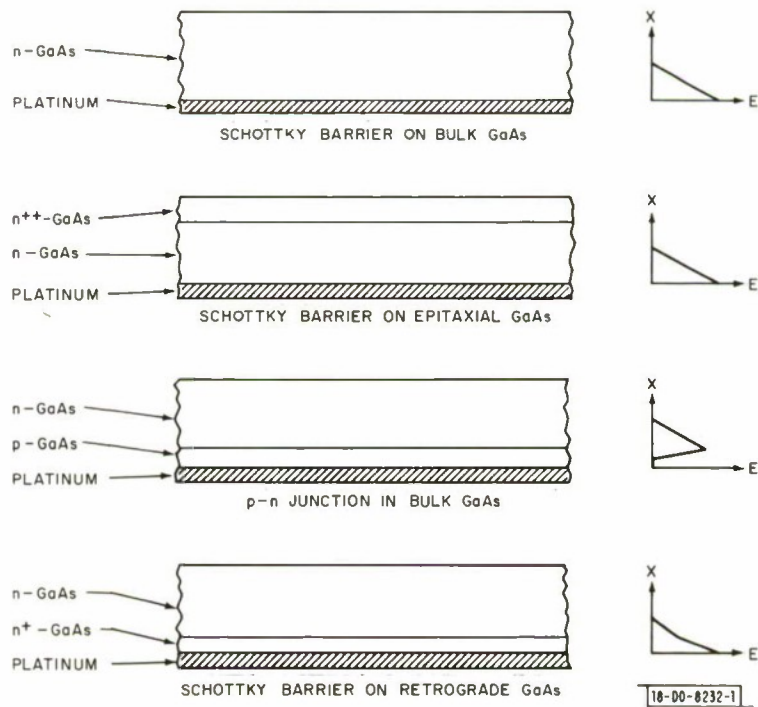
Fig.1-10. Brief summary of various K_a-bond GaAs IMPATT diodes that have been fabricated. A cross-section of each device is shown on left side of figure; a plot of electric field variation on the right. Devices made on retrograde GaAs have not as yet been tested for microwave performance.

Fig. I-11. Cross-section of the microwove circuit used for evoluotian of the K_o-band GoAs IMPATT diodes. (a) Micrawove circuit. (b) Sample contocting arrongement.

(a) MICROWAVE CIRCUIT

(b) SAMPLE CONTACTING ARRANGEMENT

18-8-10541
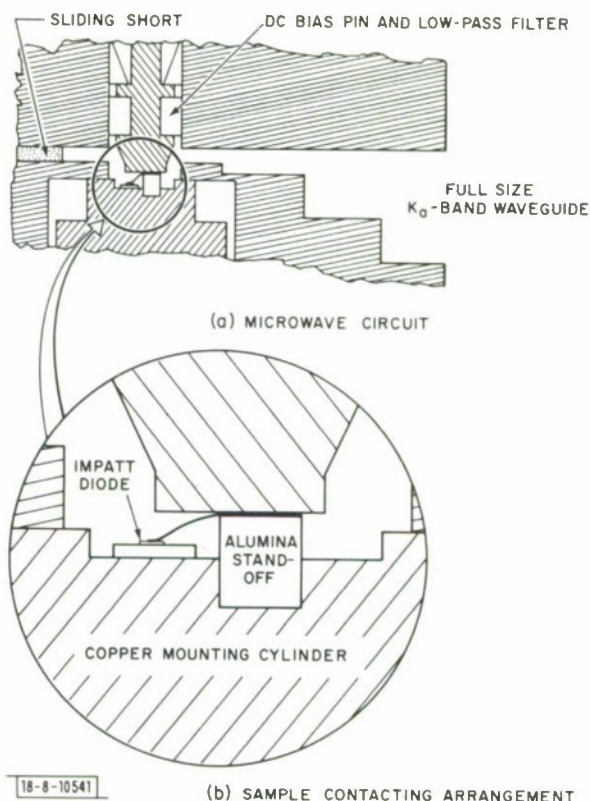
Most of the microwave results have been obtaincd in circuits similar to that shown in Fig. I-11. The copper mounting cylinder, on which the device is alloyed, is inserted into a reduced-height waveguide and the device is contacted by a spring-loadcd pin. The circuit can be tuned by means of the sliding short shown.

Results from the various devices fabricated to date are listed in Table I-1. Although these results are among the better ones, power conversion efficiencies of 6 percent are commonplace at frequencies in the 30-GHz range.

The oscillator tuning characteristic of a typical device is shown in Fig. I-12. The data points on this curve were obtained by tuning for maximum power output at each DC current setting. A characteristic of this form is cxpcctcd from normal IMPATT diode oscillator operation.
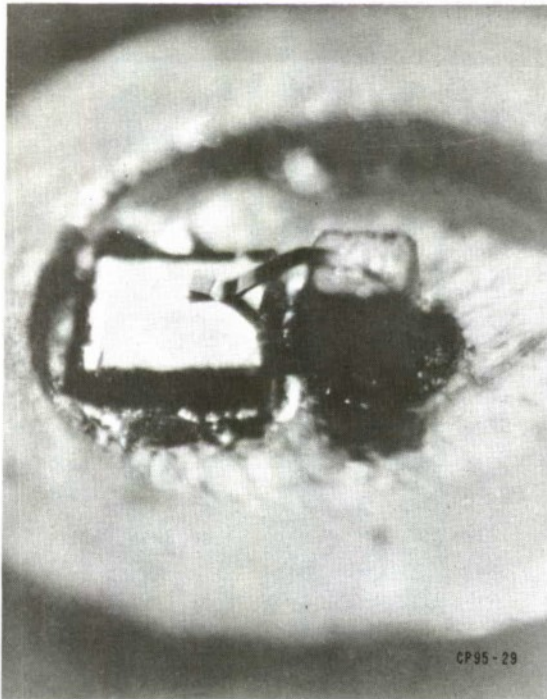
The novel aspect of this fabrication scheme is the guarding of the devices by proton bombardment. Although the suppression of edge breakdown in avalanche diodes by proton guarding. was reported somc time ago,[7] it is not obvious that the bombarded region is semi-insulating at microwave frequencies. In view of the microwave results, however, it appears that the guarded region is in fact not seriously parasitic. Another possible difficulty with proton guarding could be the tendcncy to anneal at the high operating tempcratures (200°C) of these devices. However, life tests in 300°C ovens and the prolongcd life of thc device-like reliability test structures mentioned earlier strongly indicate that there is no difficulty in this regard cither. Apparently, temperatures on the order of 700°C are necessary to anneal out the proton guarding.

A number of etchcd-mesa devices have also been made in order to compare thc proton-guarding and etched-mesa techniqucs. The microwave performancc of the two different structurcs was comparable; however, the proton guarded deviccs were clearly capable of sustaining

9

TABLE I-1

SUMMARY OF THE MICROWAVE OSCILLATOR PERFORMANCE
OF THE K_o-BAND GaAs IMPATT DEVICES FABRICATED TO DATE

Type	Power Out (mW)	Efficiency (percent)	Frequency (GHz)
Epitaxial Schottky borrier	380	6.8	28
Bulk p-n junction	320	6.7	32
Schottky barrier	250	6.4	39
Schottky borrier	280	6	30
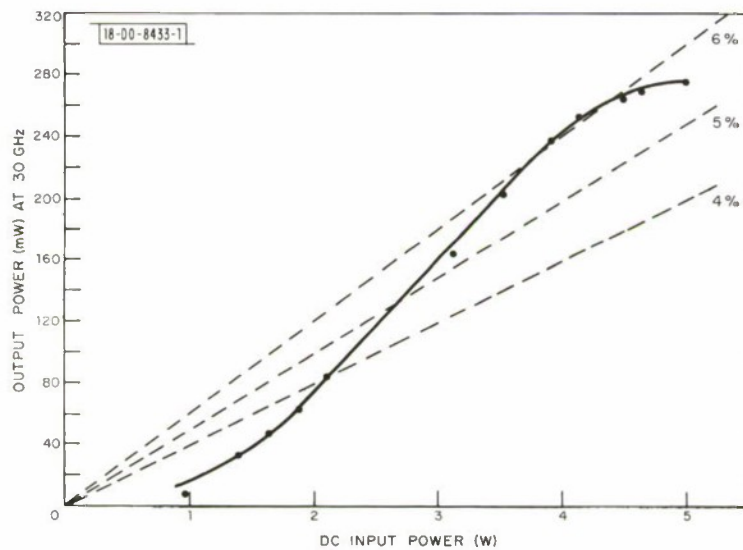
Fig. I-12. Oscillotor output pawer plotted os o function of DC input power for o K_a-band GaAs IMPATT diode aperating at 30 GHz. At each input power level, circuit tuning wos odjusted for moximum oscillotor pawer. Dashed lines shawn ore lines of constant power conversion efficiency.
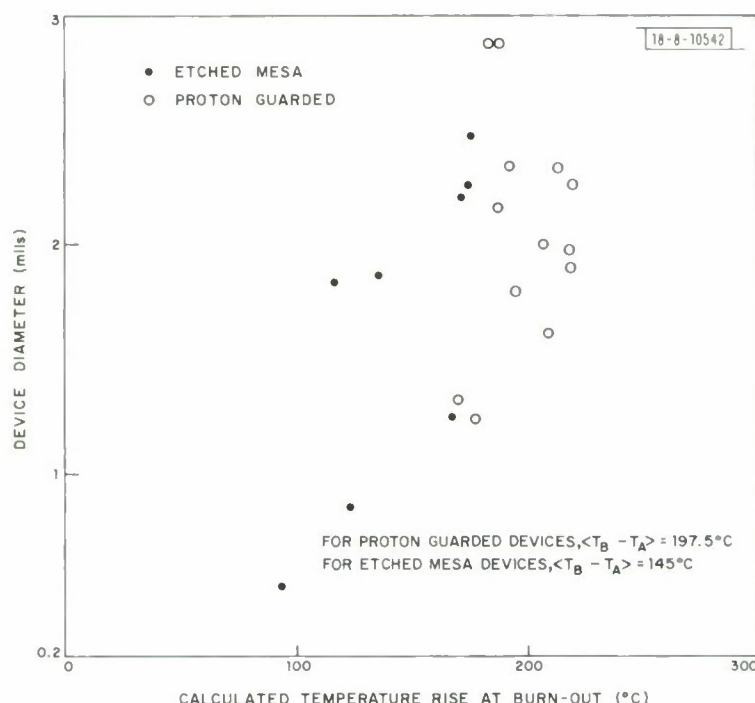
Fig. I-13. Comparison of power-handling capabilities of proton-guarded and etched-mesa K_a-band GaAs IMPATT diodes. For each device, calculated burn-out temperature is plotted on x-axis and device diameter on y-axis. Proton-bombarded devices have an average burn-out temperature approximately 50°C higher than etched-mesa devices.

higher DC powers, i.e., higher operating temperatures. Figure I-13 shows the burn-out temperatures of devices with a number of different diameters. Although some scatter exists in the data, a clear difference of 50°C on the average is observable between the burn-out temperatures of the proton-guarded and etched-mesa devices.

R. A. Murphy   C. E. Hurwitz
W. T. Lindley   J. P. Donnelly
A. G. Foyt

REFERENCES

1. D. L. Spears and H. I. Smith, Electronics Letters 8, 102 (1972).

2. Solid State Research Report, Lincoln Laboratory, M.I.T. (1971:4), p. 13, DDC AD-736501.

3. Veeco Instruments Inc., Vacuum Generators Limited Model EG-1.

4. A. Bohg, J. Electrochem. Soc. 118, 401 (1971).

5. R. M. Finne and D. L. Klein, J. Electrochem. Soc. 114, 965 (1967).

6. Solid State Research Report, Lincoln Laboratory, M.I.T. (1972:1), p. 2, DDC AD-740874.

7. A. G. Foyt, W. T. Lindley, C. M. Wolfe and J. P. Donnelly, Solid State Electronics 12, 209 (1969).

II. QUANTUM ELECTRONICS

A. OPTICALLY PUMPED ROOM TEMPERATURE GaAs LASERS

Room-temperature operation of GaAs lasers, bulk optically pumped by a tunable parametric oscillator, has been studied as a function of several variables. Cleaved platelets of GaAs were prepared either from undoped vapor-grown epitaxial layers, or from silicon-doped, Bridgman-grown crystals. These samples were pumped by light focused in a narrow rectangular image between the faces of the Fabry-Perot optical cavity in order to provide a low Fresnel number. While the peak of the laser emission for all samples occurred in the range from 0.88 to 0.89 μm, the total width of laser emission in the silicon-doped samples was significantly broader than in the pure samples. As the pump photon energy (E_p) decreased, the threshold power necessary for lasing increased. We ascribe this to two related factors:

(1) The increasing penetration of the pump radiation and the consequent decrease in excess carrier density.

(2) The lower degree of population inversion as the pump photon energy approaches the threshold quasi-Fermi level separation necessary for stimulated emission.

We have investigated both high purity GaAs ($1.6 \times 10^{14}\,cm^{-3} \leqslant N_d + N_a \leqslant 1.6 \times 10^{16}\,cm^{-3}$) and n-type, Si-doped GaAs ($N_d - N_a \simeq 5 \times 10^{18}\,cm^{-3}$). For the high purity samples, the lasing behavior did not seem to depend heavily on impurity concentration, and was more strongly a function of the surface and the cleaved-facet quality of individual samples. With a difference between pump and platelet laser photon energies of $\Delta = 0.06\,eV$, threshold power densities of 1.75 W/mil (corresponding to approximately $7 \times 10^5\,W/cm^2$) were measured. At an incident power level of twice threshold, peak power conversion efficiencies of nearly 5 percent were obtained. The lasing operation occurred with Δ as low as 25 meV (about kT at 300 K), although this presumably could be lessened if a higher pump power were used. With $\Delta = 0.06\,eV$, measurement of the far-field angular mode pattern showed a full-width, half-maximum (FWHM) power transverse angle of about 10°, corresponding to an emitting depth perpendicular to the pump face ~5 μm. At higher excitation, stimulated emission was observed over a width of 150 Å. On several n-type samples of different lengths and concentrations, measurement of the longitudinal mode spacing gave an equivalent index of refraction $\bar{n} = 4.5 \pm 0.1$.

Preliminary measurements on the Si-doped material showed marked differences from the high purity n-type samples. At the lower pump energies used on the high purity samples, the Si-doped samples were more transparent, and consequently, higher pump energies had to be used to obtain lasing. With $E_p = 1.47\,eV$ ($\Delta \simeq 0.07\,eV$), comparable thresholds (2.2 W/mil) were measured, and lasing occurred at roughly the same wavelength as before. However, at a pump power twice threshold, stimulated emission occurred over an increased range from 0.88 to 0.91 μm, a width of 300 Å, and the measured FWHM angle decreased to 6°. A typical lasing emission spectrum is shown in Fig. II-1, and a normalized power efficiency plot is shown in Fig. II-2. This material seems to be quite promising for obtaining bulk optical pumping, with the advantages of lower optical flux densities at the resonator faces and better spatial mode quality. The wide
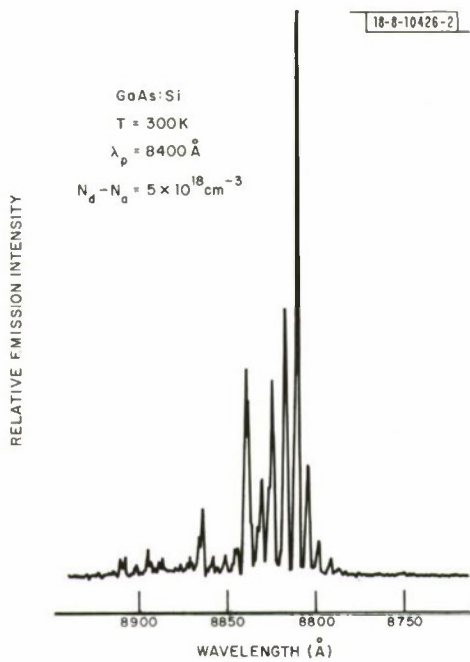
Fig. II-1. Lasing emission spectrum from GaAs:Si.
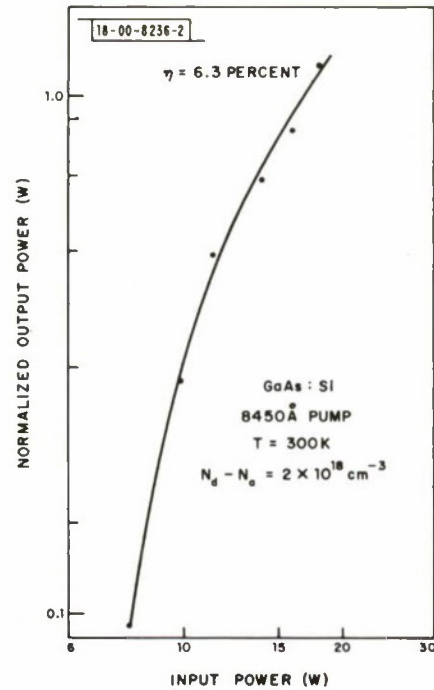
Fig. II-2. Normalized laser output power vs input pump power for a typical sample of GaAs:Si.

lasing bandwidth of the silicon-doped material also offers the possibility for tunable operation using a wavelength selector in an external cavity.

S. R. Chinn   C. M. Wolfe
J. A. Rossi   A. Mooradian

B. DOUBLE HETEROSTRUCTURE Si-DOPED GaAs LASERS

By using a GaAs-Ga_xAl_{1-x}As double heterostructure with a p-type active region of Si-doped GaAs, we have made diodes which lase at wavelengths near 9400 Å at room temperature. The diodes are operated on a pulse basis and threshold current densities are typically 10^4 A/cm^2. Output power measurements on non-optimized structures show ≤ 0.1 W laser output for currents approximately twice threshold.

The double heterostructure was grown by liquid epitaxial techniques similar to those developed elsewhere.[1] Growth of the active region (4.6 a/o Si in Ga solution) onto an n-type Ga_xAl_{1-x}As layer begins at 880°C and proceeds as the growth zone is cooled. This is followed by the usual p-type Ga_xAl_{1-x}As barrier and p-type GaAs contacting layers. Only column IV dopants are used throughout the growth process.

The spontaneous recombination of a typical diode at low injection (20 A/cm^2) is centered near 9650 Å and is more than 750 Å wide (FWHM). This transition clearly involves the deepest level (or complex) introduced by the heavy Si doping.[2] As the diode current is increased, the recombination shifts to a shorter wavelength and narrows. Finally, laser oscillation begins at 9400 Å, which is more characteristic of a transition involving the shallower Si acceptor level.[2]

The results here and elsewhere[3] show that GaAs:Si diodes can be used to obtain laser radiation at wavelengths beyond those of GaAs:Zn diodes (9000 Å). Additional device characteristics and efforts to extend the lasing wavelength still further are continuing.

<div align="right">

J. A. Rossi
J. J. Hsieh

</div>

C. INJECTION AND OPTICAL PUMPING OF InAs LASERS AT 77°K

A program has been started to pressure tune InAs lasers in the 3.1- to 2.2-μm spectral range with hydrostatic pressures up to 14 kbar. This limits the operation temperature to 77 °K and above, because the pressure transmitting fluid (helium) would solidify at lower temperatures and high pressures. A pressure generating station, high pressure sample cell and nitrogen dewar have been constructed for this purpose.

Initial tests have been conducted on InAs lasers at 77 °K in vacuum. Both optical and injection pumping of the semiconductor are feasible in the high pressure cell. Some of the spectral characteristics of the two excitation schemes are shown in Fig. II-3. The upper trace results
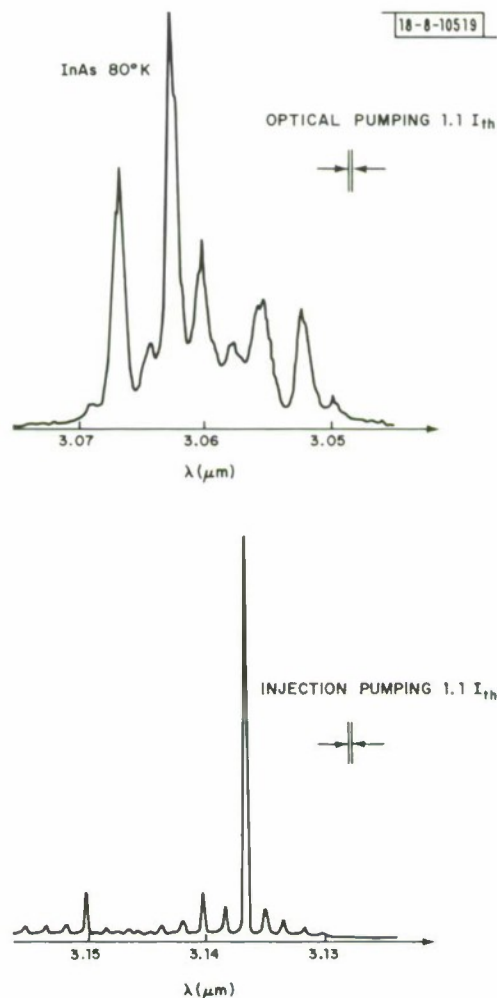

Fig. II-3. InAs optically and injection-pumped laser emission spectra.

from a bulk InAs sample, carrier concentration n $\sim 2 \times 10^{16}$ cm^{-3} with cleaved (110) faces spaced by 350 µm, indium soldered to a copper heat sink. The incident optical power at $\lambda = 1.06$ µm from a CW-pumped, repetitively Q-switched Nd:YAG laser was about 12 W cylindrically focused into an area 350×50 µm. This was about 10 percent above threshold intensity. The lower trace is obtained from a commercial InAs diode laser (Raytheon Model IAL-6) of cavity length 700 µm and width 150 µm. The injection current was 12 A, which again was ~10 percent above laser threshold. Both the optical and injection pulses were 200 nsec long with a 300-pps repetition rate.

Three features are obvious from the comparison of the two spectra.

(1) The spectral shift from 3.06 to 3.14 µm, indicating band-to-band radiation in the relatively pure bulk InAs and band-to-acceptor radiation for the heavily Zn-doped InAs diode junction.[4]

(2) Mode spacing is not 2:1 (the ratio of the cavity lengths) because of the increase of refractive index nearer the band gap.

(3) Excessive broadening of the optically pumped emission.

Actually, both types of lasers chirp to longer wavelength during the pulse time due to heating effects. The heating however is much greater for the optically pumped case, because two-thirds of the incident photon energy (1.1 eV) is lost in creating a single electron-hole pair. Very few multiple pairs (Auger processes) are evident to increase the power efficiency. On the other hand, the I^2R losses in the diode are probably an order-of-magnitude smaller than the optical-pumping conversion losses. The chirp rate for the diode is ~0.1 cm^{-1} for the 200-nsec-current pulse. For twice the threshold current, the modes noticeably broaden to ~0.5 cm^{-1}. A fast, high-repetition rate, current pulser has been constructed in order to reduce the chirp to ~0.01 cm^{-1}, a rate which would be useful for doing infrared spectroscopy.

<div align="right">A. S. Pine</div>

D. CW OPTICALLY PUMPED InSb LASER

Continuous stimulated emission has been produced in nominally pure (n $\sim 1 \times 10^{14}$ cm^{-3}) InSb between 2° and 20°K using a carbon monoxide laser to resonantly excite in a collinear pump geometry. Laser emission occurred at 5.27 µm with an output power of 10 mW in a single axial mode. Laser emission with less output power was also observed at 5.45 µm, which corresponds to a zinc impurity transition. The sample mode volume in both cases was about 300 µm long × 100 µm in diameter.

<div align="right">A. Mooradian
S. R. J. Brueck</div>

E. InSb OPTICAL CONVERTER

An InSb laser rod $1 \times 0.03 \times 0.03$ cm has been optically pumped with two arrays (25 diodes each) of GaAs diode lasers. The device, shown in Fig. II-4, operated with average output powers of up to 50 mW at a temperature of 10°K. Mode spacings were unresolved with a conventional spectrometer because of the 1-cm cavity length. Overall lasing bandwidth was about 2 cm^{-1}, which was about half the spontaneous linewidth measured normal to the lasing direction for pump levels below laser threshold. This device has a considerably larger mode volume than conventional diode lasers of InSb, which would account for the higher average output power levels. Volume excitation of the InSb rod relies on the long diffusion lengths for excited carriers in InSb at low temperature.

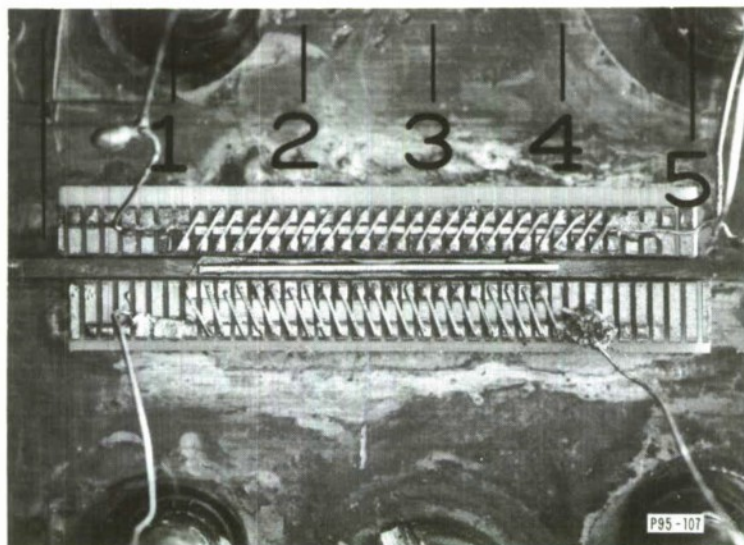<div align="right">A. Mooradian
J. A. Rossi</div>

Fig. II-4. GaAs diode laser array pumped rod of InSb. Scale is in tenths of an inch.

F. TUNING CHARACTERISTICS OF A LOW DENSITY, SPIN-FLIP LASER

A low concentration (n = 7 to 9×10^{14} cm^{-3}) InSb spin-flip Raman laser has been operated at low magnetic fields (1 to 14 kG) in an electromagnet. The spin-flip scattering was pumped with a CW CO laser ($\lambda \approx 5.3\,\mu$m) and the samples were immersed in superfluid helium (2°K). The tuning rate of the spin-flip laser output frequency with magnetic field was measured by hetero-dyning the output of the spin-flip laser with a second stable CO laser. A liquid helium cooled, Cu:Ge photoconductor was used as the heterodyne detector. The observed tuning rate was 48 ± 2 MHz/G. This should be compared with the tuning rate of the spontaneous spin-flip radiation (70 MHz/G) and with the tuning rate of 16 MHz/G previously reported[5] for an InSb sample of concentration n = 1×10^{16} cm^{-3} at a higher magnetic field of 35 kG. These different tuning rates can be understood on the basis of mode pulling effects between the InSb sample cavity resonant frequencies and the spontaneous spin-flip Raman frequency. As previously noted,[5] this mode pulling phenomenon is described by the equation

$$\nu = \frac{\nu_c \Gamma_o + \nu_o \Gamma_c}{\Gamma_o + \Gamma_e} \qquad (II-1)$$

where ν is the actual frequency of oscillation, and ν_c and ν_o are the peaks of the cavity and spontaneous scattering resonances, respectively. Here Γ_o is the linewidth of the spontaneous spin-flip scattering, which has been assumed Lorentzian, and Γ_e is the cavity linewidth. The spontaneous linewidth Γ_o is expected to be narrower in the present lower density samples because of the reduced effects of nonparabolicity broadening[6] and, correspondingly, the tuning rate with magnetic field should more closely follow the spontaneous tuning rate, as is experimentally observed.

Calculated magnetic field tuning rates as a function of the spontaneous linewidth are shown in Table II-1, along with calculated values for the discontinuous frequency jump between modes $\Delta\nu$ and the percentage of the frequency axis covered by a single laser. In these calculations, a sample length of 6 cm was used, as were the values for the frequency and magnetic field derivatives of

Γ_o (cm^{-1})	$d\nu/dH$ (MHz/G)	$(d\nu/dH)\,\Delta H$ (GHz)	$\Delta\nu$ (GHz)	Percent Frequency Range Covered
		TABLE II-1		
		CALCULATED TUNING CHARACTERISTIC OF SPIN-FLIP LASER		
0.01	63	5.4	0.6	91
0.04	48	4.1	1.8	69
0.10	33	2.8	3.1	47
0.30	15	1.3	4.5	22
0.50	10	0.8	5.0	13
1.00	5	0.4	5.4	7

-00-8452-1

PRESSURE = 1 torr
T = 300K

360 MHz
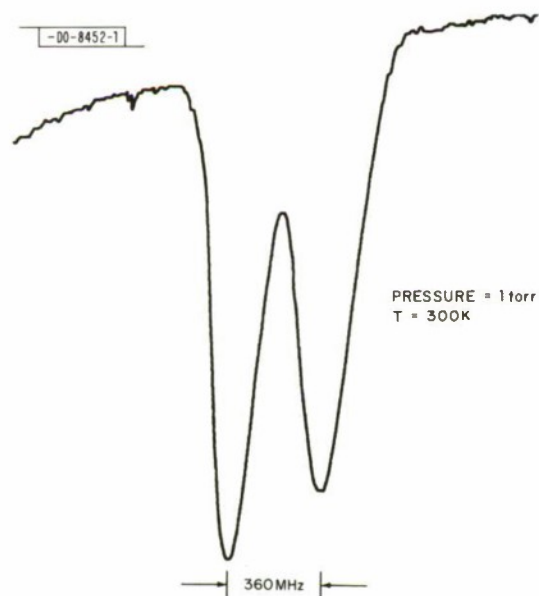
Fig. II-5. Absorption spectrum of the NO R(1/2)$_{1/2}$ transition: $\lambda = 5.2\,\mu$m, cell length = 10 cm, $P \approx 1$ torr.

the index of refraction found previously.[5] A spontaneous linewidth of 0.04 cm^{-1} gives a tuning rate comparable to that observed experimentally.

The extremely low observed threshold powers of less than 5 mW inside the sample, as compared with 50 mW in the higher density sample, provide an independent check on this value of the spontaneous linewidth. Due to the lower magnetic field operation, the resonance enhancement of the spontaneous spin-flip scattering cross section (R ≈ 2000) is approximately an order-of-magnitude higher than in the high field case and just compensates for the smaller number of electrons. This implies that the spontaneous linewidth in the 7 to 9×10^{15} cm^{-3} sample is approximately a factor-of-ten lower than in the 1×10^{16} cm^{-3} sample, in agreement with the results deduced from the tuning rate measurements.

The absolute frequency stability of the spin-flip laser was also measured by the heterodyne technique; the short-term frequency drifts were less than 2 MHz in 1 sec. The spin-flip laser is therefore more than adequate for absorption spectroscopy of low pressure molecular gases in the infrared, which have Doppler-limited absorption linewidths on the order of 100 MHz. As an illustration of this application for the spin-flip laser, the absorption spectrum of the R(1/2)$_{1/2}$ line of nitric oxide (NO) has been obtained and is shown in Fig. II-5. The gas pressure in a 10-cm cell was approximately 1 torr and consequently the observed linewidths are Doppler-limited. The λ-type doubling of this NO vibration-rotation transition, resulting from the interaction of the electronic and molecular angular moments, is completely resolved. The relative strength and width of the two lines result from the hyperfine splitting of the NO transition.

S. R. J. Brueck
E. J. Johnson
A. Mooradian

G. PRESSURE BROADENING OF A WATER VAPOR LINE NEAR 5.3 μm

Using a temperature-tunable, CW, $PbS_{0.6}Se_{0.4}$ semiconductor diode laser[7] and a multiple-pass White cell, we have measured the self- and nitrogen-pressure broadenings of the 1879.01 cm^{-1} water vapor line.[8] Because it has the narrowest width of any water vapor line yet observed,[9] it was chosen for detailed study.

The diode laser was mounted on a 10°K conduction-cooled heat sink in a liquid helium dewar, at which temperature the threshold current was 170 mA. However, it was necessary to operate the laser at nearly five times threshold current in order to tune its frequency to the water vapor line of interest. The output power of the laser axial mode used was estimated to be about 30 μW. The beam was collimated by a 4-inch focal length lens and only the central portion of the beam, having a diameter of about $\frac{1}{2}$-inch, was directed to the entrance port of a White cell,[10] which has aluminum spherical mirrors with 1.5-m radius of curvature and which had been adjusted for eight passes, thus yielding a total optical path length of 12 m. The transmittance of the evacuated White cell was over 50 percent; the loss included four Fresnel reflection losses by the barium fluoride windows. In the near future, the use of gold mirrors will increase the transmittance by about 50 percent. The laser beam was chopped at 400 Hz before it entered the entrance slit of a Perkin-Elmer grating spectrometer with spectral resolution about 0.5 cm^{-1}, just about narrow enough to filter out the adjacent axial modes which are spaced 1.0 cm^{-1} from the desired mode. The exit beam from the spectrometer was detected by a Ge:Au detector, synchronously amplified and recorded as a function of diode current.

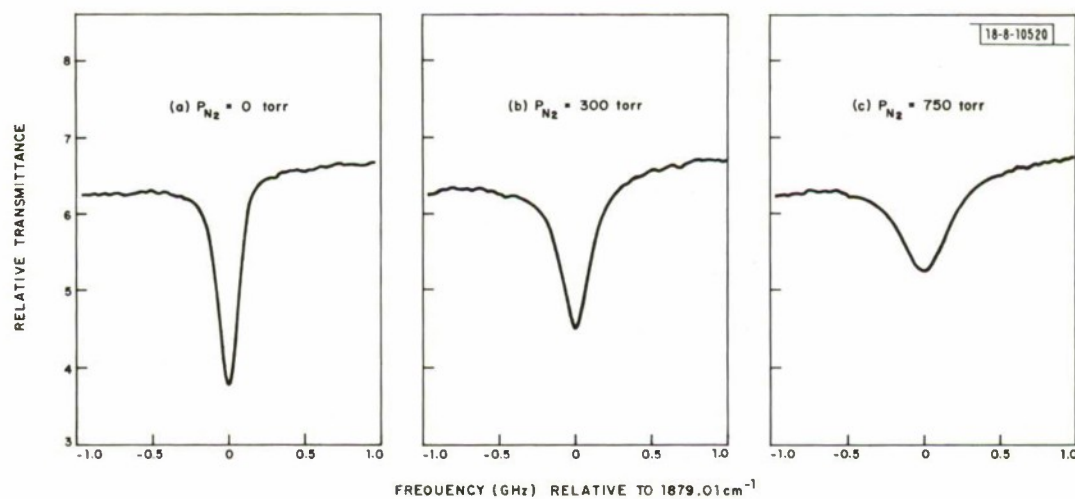Fig. II-6. Water vopor-nitrogen pressure broadening (P_{H_2O} = 1. 95 torr).
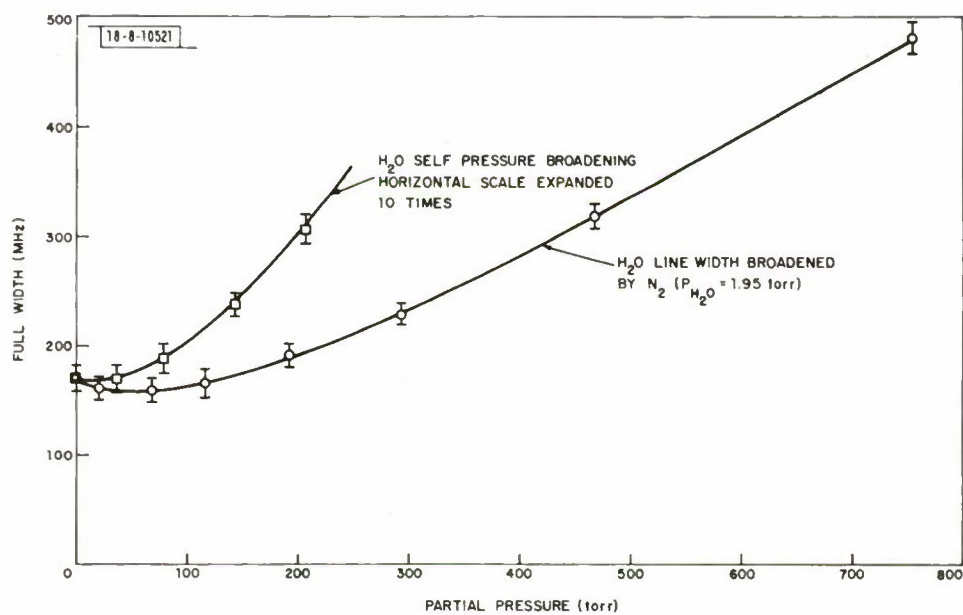

Fig. II-7. Water vapor line widths vs broadening pressure.

Figure II-6 shows the recorder traces of the nitrogen broadening of the water vapor line for three different total pressures. Distilled water and Matheson prepurified grade N_2 (purity 99.997 percent) were used. The extreme dryness of the nitrogen gas was verified by noting that the recorder traces over the frequency of the water vapor line remained the same in going from an evacuated cell case to a N_2-filled cell case. The horizontal scale was originally in diode current but was converted to frequency using the tuning rate of the laser. This tuning rate was determined by plotting the frequency of an axial mode vs diode current and also by measuring the nitric-oxide, λ-doubling spacing ($0.0119 \, \text{cm}^{-1}$) at $1871 \, \text{cm}^{-1}$. Both of these methods yielded a tuning rate of $0.00868 \pm 0.00008 \, \text{cm}^{-1}/\text{mA}$.

Figure II-7 is a plot of the full linewidth at one-half absorption vs total gas pressure for water and N_2 broadening. In the case of nitrogen broadening, the water vapor pressure was maintained at 1.95 torr throughout the experiment. The estimated errors are largest near atmospheric pressure, because the width (being dependent on how well one can estimate at line center the transmittance of an evacuated cell) changes most rapidly with the estimated transmittance. It is to be noted that the horizontal scale for the self-broadening plot is expanded ten times. The rate of self broadening is twenty-five times that of nitrogen broadening. This can be compared with a 5:1 ratio of self:nitrogen broadening found for the 2.7-μm band.[11] The much greater self broadening of the water vapor line is due to the much stronger, long-range, dipole-dipole interaction[12] occurring in general among polar molecules such as water. Since N_2 is nonpolar, its interaction with the water molecule is of the dipole-quadrupole type and is therefore much weaker in magnitude.

Although we have studied in detail only one water vapor line, namely, the 1879.01-cm^{-1} line, the diode laser was tunable over at least a dozen other water lines. A few of these have been observed and are listed in Table II-2. Detailed study of water vapor over a more extended region

TABLE II-2		
OBSERVED H_2O LINES WITH $PbS_{0.6}Se_{0.4}$ DIODE LASER		
Frequency[8] (cm^{-1})	Line Intensity[8] $(\text{cm}^{-1}/\text{g-cm}^{-2})$	Ratational Transition[8] $(J'_{K'_a K'_c} \leftarrow J''_{K''_a K''_c})$
1858.55	60.52	$9_{3,7} \leftarrow 8_{2,6}$
1860.94	12.32	$12_{1,11} \leftarrow 11_{2,10}$
1861.56	37.02	$12_{2,11} \leftarrow 11_{1,10}$
1864.05	5.95	$15_{0,15} \leftarrow 14_{1,14}$
1870.83	79.46	$10_{3,8} \leftarrow 9_{2,7}$
1879.01	1.58	$16_{1,16} \leftarrow 15_{0,15}$
1879.34	12.12	$13_{1,12} \leftarrow 12_{2,11}$
1879.60	4.04	$13_{2,12} \leftarrow 12_{1,11}$

can be accomplished by employing a magnetic field for coarse tuning and using the diode current for fine tuning. Finally, by extending the study to include the mixtures, H_2O-O_2, H_2O-CO_2, and H_2O-O_3, etc., the result will be directly applicable to problems in atmospheric transmission.

R. Eng   A. Mooradian
P. L. Kelley   A. R. Calawa

REFERENCES

1. M. B. Panish, S. Sumski and l. Hayashi, Metallurgical Trans. 2, 795 (1971).

2. H. Kressel, J. U. Dunse, H. Nelson and F. Z. Hawrylo, J. Appl. Phys. 39, 2006 (1968).

3. B. H. Ahn, C. W. Trussell and R. R. Shurtz, Appl. Phys. Letters 19, 408 (1971).

4. l. Melngailis and R. H. Rediker, J. Appl. Phys. 37, 899 (1966), DDC AD-642173.

5. S. R. J. Brueck and A. Mooradian, Appl. Phys. Letters 18, 229 (1971), DDC AD-729611.

6. S. R. J. Brueck and F. A. Blum (to be published).

7. K. W. Nill, F. A. Blum, A. R. Calawa and T. C. Harman, Appl. Phys. Letters 19, 79 (1971), DDC AD-734114.

8. W. S. Benedict and R. F. Calfee, Line Parameters for the 1.9 and 6.3 Micron Water Vapor Bands (Government Printing Office, Washington, D.C. 1967).

9. Solid State Research Report, Lincoln Laboratory, M. l. T. (1972:1), p. 15, DDC AD-740874.

10. E. R. Stephens, Appl. Spectry. 12, 80 (1958).

11. D. E. Barch, D. A. Gryvnak and R. R. Patty, Absorption by H_2O Between 2800 and 4500 cm-1 (2.7 Micron Region), private communication.

12. J. O. Hirschfelder, C. F. Curtiss and R. B. Bird, Molecular Theory of Gases and Liquids (John Wiley and Sons, 1954).

III. MATERIALS RESEARCH

A. FREE-CARRIER ABSORPTION IN n-TYPE CdTe

In order to investigate the free-carrier absorption (FCA) in n-type CdTe, the optical transmission of samples with carrier concentrations between 3.6×10^{16} and $1.8 \times 10^{18}\,cm^{-3}$ has been measured at room temperature for wavelengths between $0.9\,\mu m$ (the location of the intrinsic absorption edge) and $12\,\mu m$. The samples were single crystal specimens cut from ingots grown by the vertical Bridgman method from melts doped with donor impurities (Al, Ga, In, Cl, Br or I).

The absorption between 2 and $12\,\mu m$ is due predominantly to intraband FCA. The experimental data in this wavelength region for five representative samples covering the entire concentration range are shown in Fig. III-1, where the absorption coefficient (α) is plotted against wavelength (λ) on a log-log scale. For all these samples, as well as for those not included in the figure, the data are very well represented by straight lines, although in some cases there are small deviations at the shorter wavelengths. Thus α is proportional to λ^p, where p is a constant for each sample. (This is the wavelength dependence characteristic of intraband FCA.) As expected for FCA, α at a given wavelength increases with carrier concentration (n). The quantitative dependence is shown in Fig. III-2, where the values of α at 4, 6, 8 and $10\,\mu m$ for all the samples are plotted against n on a log-log scale. Once again the data are very well represented by straight lines. This demonstrates the consistency between the results for the different samples.
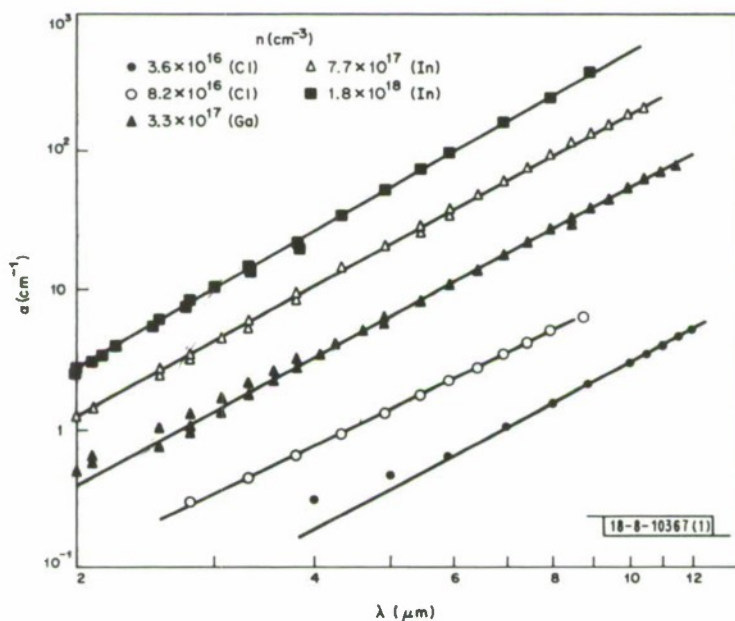

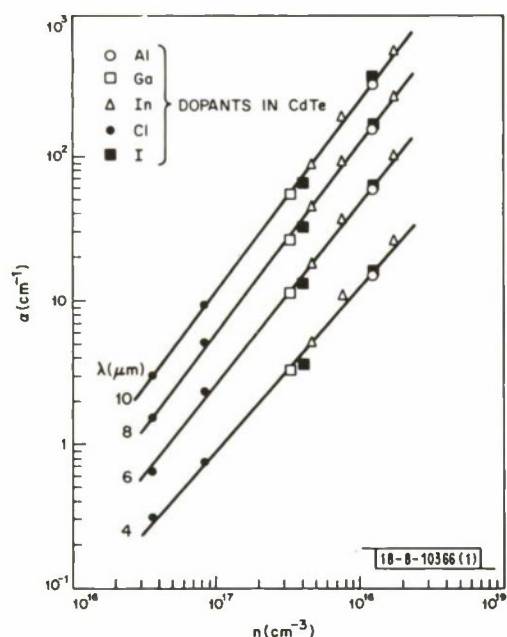Fig. III-1. Room temperature absorption coefficient (α) as a function of wavelength (λ) between 2 and 12 μm for representative samples of n-type CdTe.

Fig. III-2. Room temperature absorption coefficient (α) at wavelengths of 4, 6, 8, and 10 μm as a function of carrier concentration (n) for n-type CdTe.

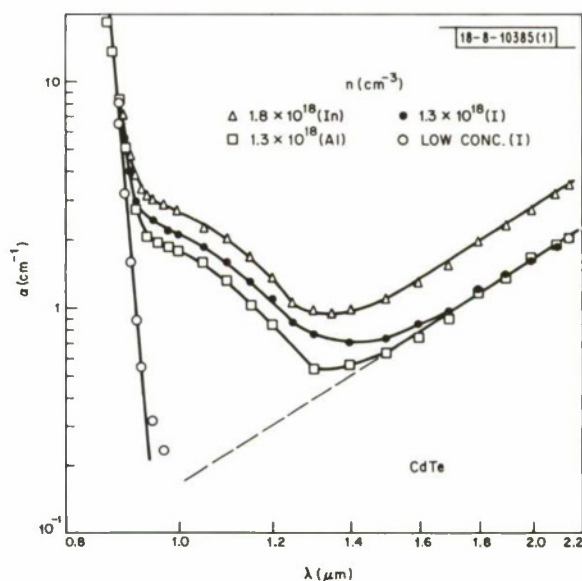Fig. III-3. Room temperature absorption coefficient (α) as a function of wavelength (λ) between 0.9 and 2 μm for our three most heavily doped samples of n-type CdTe, together with absorption edge data for a low-carrier-concentration sample doped with I and compensated by native acceptors.

Although the absorption between 2 and 12 μm is due to intraband FCA, the dependence of α on n and λ differs quantitatively from the predictions of the classical expression for this process. According to this expression, α is proportional to $n\lambda^2$, but the observed dependence on n is superlinear rather than linear, and the exponent p in λ^p varies from sample to sample between 2.7 and 3.4. Similar values of p have been obtained for CdTe by various workers.[1] These values are consistent with quantum mechanical treatments of intraband FCA, if the carrier scattering associated with absorption is attributed to a combination of polar optical mode scattering, which is known to dominate the electron lattice mobility at room temperature, and ionized impurity scattering.

The absorption observed between 2 μm and the beginning of the intrinsic absorption edge becomes significantly greater than the intraband FCA extrapolated from the 2 to 12-μm region. The additional absorption is illustrated in Fig. III-3, which shows the data for our three samples with highest n, doped respectively with Al, In and I, together with absorption-edge data for a high resistivity sample doped with I and compensated by native acceptor defects. The absorption curves for the three high concentration samples all rise markedly at about 1.3 μm, and the absorption cross sections (α/n) are about the same. This qualitative and quantitative similarity in the curves for samples heavily doped with three different impurities suggests that the additional absorption is due to another free-carrier process, specifically interband FCA associated with electron transitions from the Γ-conduction-band minimum to higher minima.
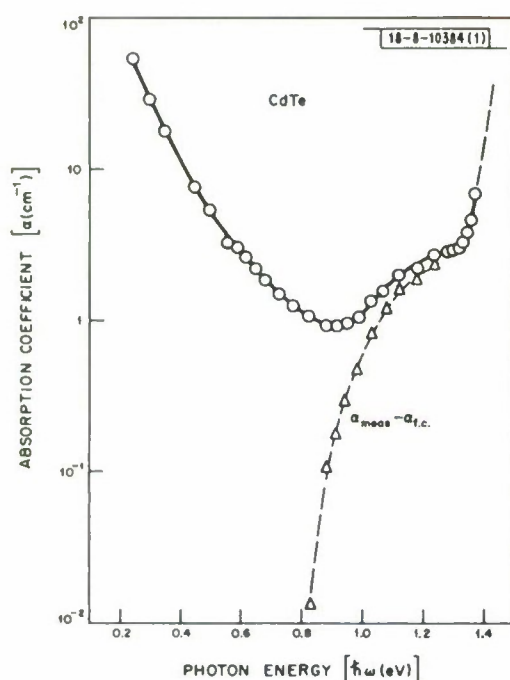
Fig. III-4. (a) Room temperature absorption coefficient (o) as a function of photon energy for our most heavily doped sample of n-type CdTe, and the differences between the measured values and those for intraband FCA found by extrapolation.
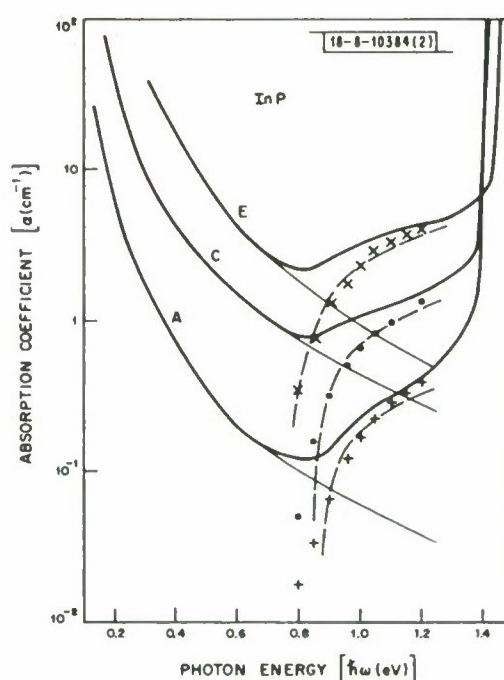
Fig. III-4. (b) Similar plots for 3 samples of n-type InP [from Dumke, Lorenz and Pettit (Ref. 2)].

This explanation for the additional absorption is supported by the strong similarity between our data for CdTe and those for interband FCA in n-type InP reported by Dumke, Lorenz and Pettit.[2] The two sets of results are compared in Figs. III-4 (a and b), where α is plotted against photon energy instead of wavelength. Figure III-4(a) shows the data for our most heavily doped sample. The solid line gives the measured values for α, while the dashed line gives the differences between these values and those for intraband FCA found by extrapolation. Figure III-4(b) is a similar plot for 3 samples of n-type InP, reproduced from the paper of Dumke, et al.[2] In this case, the dashed lines are theoretical curves which these authors calculated for interband FCA, while the points on these lines are those obtained from the experimental data by subtraction of the extrapolated values for intraband FCA. The interband curve for their sample C (n = 1.65 × 10^{18} cm^{-3}) is strikingly similar to the one for our sample (n = 1.8 × 10^{18} cm^{-3}), although the values of α at the highest energies are about a factor of 2 lower than ours. Therefore, we believe that the additional absorption in our sample is quite probably due to interband transitions, and furthermore that the conduction band energy separation in CdTe (which has not been measured previously) is almost the same as the separation involved in the interband FCA in InP. Onton, Yacoby and Chicotka[3] have recently measured the InP separation ($\Gamma \rightarrow X$) to be 0.96 eV.

Although the combination of interband and intraband FCA adequately explains the absorption between 0.9 and 2 μm in our most highly doped samples, it is not sufficient to account for the

absorption in this region by many of the lower concentration samples. For these samples, the curves of absorption cross section against wavelength vary so much, both qualitatively and quantitatively, that no definite conclusion can be drawn concerning even the number of additional absorption processes that are involved. However, the observation of relatively high absorption cross sections for Cl-doped samples suggests that one process might be the excitation of electrons from occupied Cl donor levels[4] to the conduction band.

A. J. Strauss
G. W. Iseler

B. PREPARATION OF $NaYF_4$:Yb, Er FOR INFRARED-TO-VISIBLE UPCONVERSION

Independent studies at our laboratory[5] and elsewhere[6,7] have recently shown that $NaYF_4$ with Y partially replaced by Yb and Er is a very promising phosphor for upconversion of near-infrared ($\sim 0.98\mu m$) to green ($\sim 0.54\mu m$) radiation. In order to determine the best method for producing this phosphor, we have compared the efficiencies of samples prepared in several different ways. All samples had the nominal composition $NaY_{0.8}Yb_{0.18}Er_{0.02}F_4$. This composition was selected because preliminary experiments showed it to exhibit relatively high efficiencies, but detailed experiments to determine the optimum composition have not yet been performed.

The starting materials used for synthesis are NaF and the fluorides of the three rare earths. Although the compound can be prepared from stoichiometric mixtures, in which the number of moles of NaF is equal to the total number of moles of the rare earth fluorides, the upconversion efficiency is found to be much higher for samples prepared from mixtures containing a considerable amount of excess NaF. This difference can be explained in terms of the pseudobinary phase diagram for the NaF-YF_3 system,[8] which is shown in Fig. III-5. (Apparently the diagram is not greatly changed by substitution of relatively small amounts of Yb and Er for Y.) At 691°C, $NaYF_4$ is transformed from a high-temperature phase with cubic fluorite structure to a low-temperature phase with hexagonal structure. Since the liquidus temperature for the stoichiometric composition is 930°C, samples of $NaYF_4$ prepared from a stoichiometric melt crystallize in the cubic phase and transform into the hexagonal phase on cooling. However, samples prepared from melts containing less than 32-mole-percent YF_3 do not undergo this transformation, since the liquidus temperatures for these compositions are below 691°C and consequently the $NaYF_4$ crystallizes directly in the hexagonal form. These are the samples with the highest upconversion efficiencies. We attribute the reduction in efficiency for the samples prepared from stoichiometric melts to the presence of lattice defects resulting from the cubic-to-hexagonal transformation. The creation of significant defect concentrations would not be surprising in view of the rather drastic difference in structure between the two phases, which differ in density by about 10 percent.[9]

Samples of $NaYF_4$:Yb, Er which have not undergone the phase transformation can be synthesized by solid state reaction between the component fluorides at temperatures below the transformation temperature. In an attempt to obtain improved upconversion efficiency by this method, we have prepared phosphors by firing stoichiometric fluoride mixtures between 450 and 650°C, but their efficiencies are low. The x-ray diffraction lines for these samples are considerably broader than those for samples obtained from either stoichiometric or NaF-rich melts, indicating that lower crystal perfection is again responsible for the reduced efficiency.

A LIQUID

B NaF + LIQUID

C NaF + HEXAGONAL NaF·YF$_3$

D HEXAGONAL NaF·YF$_3$ + LIQUID

E FLUORITE CUBIC NaF·YF$_3$ – 5NaF·9YF$_3$ SOLID SOLUTION + LIQUID

F FLUORITE CUBIC NaF·YF$_3$ – 5NaF·9YF$_3$ SOLID SOLUTION

G HEXAGONAL NaF·YF$_3$ ss + CUBIC NaF·YF$_3$ – 5NaF·YF$_3$ ss

H CUBIC NaF·YF$_3$ – 5NaF·9YF$_3$ ss + ORDERED 5NaF·9YF$_3$ ss

I HEXAGONAL NaF·YF$_3$ ss

J HEXAGONAL NaF·YF$_3$ ss + ORDERED 5NaF·9YF$_3$ ss

K ORDERED 5NaF·9YF$_3$ ss

L HEXAGONAL NaF·YF$_3$ ss + ORTHORHOMBIC YF$_3$

M ORDERED 5NaF·9YF$_3$ + ORTHORHOMBIC YF$_3$

N CUBIC 5NaF·9YF$_3$ + ORTHORHOMBIC YF$_3$

O ORTHORHOMBIC YF$_3$ + LIQUID
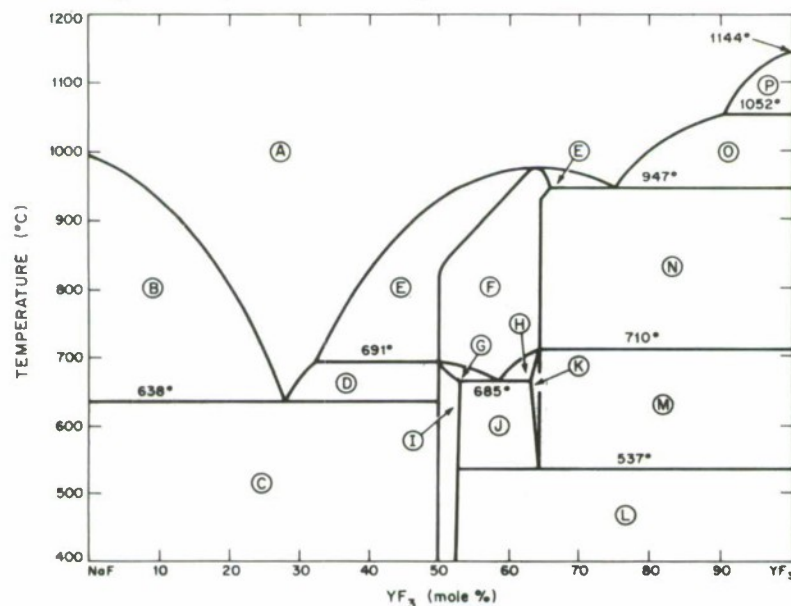
P HIGH-TEMPERATURE YF$_3$ + LIQUID

Fig. III-5. Pseudobinary phase diagram of the NaF–YF$_3$ system (Ref. 8).

Our most efficient phosphors have been prepared by the following procedure. Each of the rare earth fluorides (YF$_3$ of nominal 6 9's purity, YbF$_3$ and ErF$_3$ of nominal 5 9's purity, supplied by Research Chemicals) is first heated to 750°C in a stream of HF gas to assure complete fluorination and removal of oxygen. The purified compounds in the desired proportions are mixed with a 20 to 100 wt% excess of dried NaF (nominal 5 9's purity, supplied by Semi-Elements, Inc.). The mixture is placed in a platinum boat and heated in a resistance furnace, first to 200°C for 16 hours and then to 1000°C for about 6 hours. The furnace is turned off and allowed to cool to room temperature. Both heating and cooling are performed with the sample under flowing argon, which is first passed through a bed of titanium chips at 800°C to remove oxygen and water vapor. The cooled product is crushed in an agate mortar (not ground, because grinding reduces the upconversion efficiency, probably by introducing defects due to work damage). Finally the sample is leached repeatedly with boiling water until its x-ray diffraction pattern no longer shows peaks characteristic of NaF.

J. W. Pierce
E. J. Delancy

C. CRYSTAL CHEMISTRY OF M$^+$SbO$_3$ COMPOUNDS

Unlike the M$^+$NbO$_3$ and M$^+$TaO$_3$ compounds, the M$^+$SbO$_3$ compounds do not form structures having 5$^+$ cations on opposite sides of an anion. Thus, KSbO$_3$ does not form the cubic perovskite

structure. At atmospheric pressure it generally has the rhombohedral ilmenite structure. However, Spiegelberg[10] reported synthesizing two cubic phases of $KSbO_3$ by annealing for 3 weeks at 1000°C. One of these was primitive, with space group Pn3. The other was body-centered, but Spiegelberg was unable to determine its space group.

In the primitive cubic $KSbO_3$, pairs of SbO_6 octahedra share common edges to form Sb_2O_{10} clusters.[10] These clusters share corners to form the network shown in Fig. III-6. The network contains empty tunnels of face-shared octahedra that run parallel to the ⟨111⟩ directions and intersect at the center of the front face in Fig. III-6. This origin is itself a large octahedral interstice, and along any ⟨111⟩ direction there are three additional octahedral positions between the origin and its body-center equivalent. Each of the shared faces along the tunnels consists of either O_1 or O_2 oxygen atoms. The order of the faces is O_1-O_2-O_2-O_1, and the triangular area of an O_1 face is somewhat larger than that of an O_2 face. The primitive unit cell contains $K_{12}Sb_{12}O_{36}$, and the K^+ ions are ordered within the octahedral sites of these tunnels: eight in O_1-O_2 octahedra along four tetrahedral directions from the origin, and four in O_2-O_2 octahedra along the remaining four directions.

The body-centered cell is closely related to the primitive unit cell. A body-centered cubic I23 phase containing a network similar to the one in Fig. III-6 has been reported[11,12] for $La_4ORe_6O_{18}$. In this structure, an oxygen is located at the origin, and four La^{3+} ions occupy O_1-O_2 octahedra in [111], [$\bar{1}11$], [$\bar{1}1\bar{1}$], [$1\bar{1}1$] directions. It is therefore reasonable to assume that the body-centered form of $KSbO_3$ contains the SbO_3 network of Fig. III-6 with the K^+ ions disordered over the octahedral sites of the tunnels. This assignment gives space group Im3.
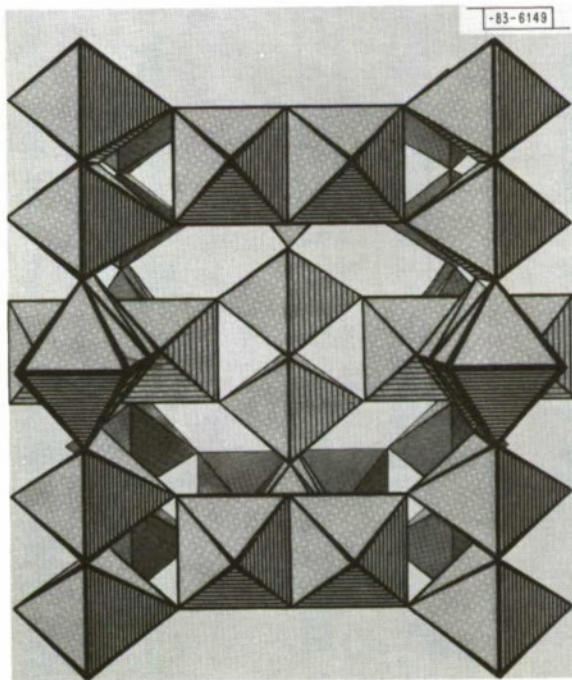

Fig. III-6. The $Sb_{12}O_{36}$ network of the unit cell in cubic $KSbO_3$.

The primitive and body-centered forms of $KSbO_3$ and $RbSbO_3$, as well as a distorted-cubic form of $TlSbO_3$, were easily prepared at high pressures by Kafalas.[13] However, attempts to prepare $NaSbO_3$, $AgSbO_3$ and $LiSbO_3$ by the same technique gave, respectively, an ilmenite, a pyrochlore and an orthorhombic phase. We have been able to prepare each of these compounds in the body-centered Im3 phase by an ion-exchange method. A cubic $KSbO_3$ phase was mixed for a few hours with molten MNO_3 (M = Li, Na, Rb or Ag) in about 1:10 molar ratio. In each case, the K^+ ions appeared to be completely replaced by the M^+ ions, since the x-ray powder pattern showed significant changes in the cell parameters. Except for $AgSbO_3$, the process is reversible. If one of the other $MSbO_3$ phases is mixed with molten KNO_3, the Im3 $KSbO_3$ phase is recovered.

TABLE III-1	
LATTICE CONSTANTS OF $MSbO_3$ POLYMORPHS WITH SPACE GROUP Im3	
Compound	a (Å)
$AgSbO_3$	9.4038
$LiSbO_3$	9.4655
$NaSbO_3$	9.3775
$KSbO_3$	9.5632
$RbSbO_3$	9.6985

Table III-1 shows the lattice constants, obtained from powder and single-crystal x-ray data, for the various $MSbO_3$ polymorphs having space group Im3. With the exception of $LiSbO_3$, the lattice constants scale with the M-ion radii. The $LiSbO_3$ parameter shows a marked expansion, which we interpret to indicate that the Li^+ ion occupies the center of an O_2-ion face rather than an octahedral site.

Single crystals of $NaSbO_3$ and $AgSbO_3$ were prepared by ion exchange of $TlSbO_3$ with molten $NaNO_3$ and $AgNO_3$, respectively. Weissenberg photographs of both crystals showed low-symmetry cubic Im3. Systematic absences were observed for h + k + l = 2n + 1, consistent with space groups I23, $I2_13$ and Im3. X-ray intensity measurements of three-dimensional data to $2\Theta = 60°$ were taken with a G.E. XRD-5 diffractometer using Zr-filtered $MoK\alpha$ radiation at 5° take-off angle. Each peak height was counted for 10 sec, and backgrounds were counted for 10 sec at ±2° in 2Θ off the peak. The Lorentz polarization correction and a ϕ-angle absorption correction were applied. From the strong similarity between primitive and body-centered $KSbO_3$ powder intensities and the ion-exchange experiments, it was assumed that the SbO_3 network is the same for both structures. The Sb^{5+}-ion and O^{2-}-ion positions for the Pn3 form of $KSbO_3$ (Ref. 10) were used for initial refinement with a least-squares program to give a reliability factor R = 0.17 for $NaSbO_3$ and R = 0.18 for $AgSbO_3$. From the calculated structure factors based on this model, a Fourier map clearly revealed the positions of the Na^+ and Ag^+ ions. These positions exhibited a mirror plane perpendicular to the cubic axes, which indicates that Im3 is the correct space

TABLE III-2 ATOMIC POSITIONS AND THERMAL PARAMETERS OF $NaSbO_3$				
Atom Position	Sb 12e	O_1 12d	O_2 24g	Na 16f
Multiplier	1/4	1/4	1/2	$1/3 \times 0.81(3)$*
X	0.8384(2)	0.356(2)	0	0.1229(9)
Y	0	0	0.334(1)	0.1229(9)
Z	1/2	0	0.287(1)	0.1229(9)
β_{11}	0.0014(2)	0.006(3)	0.000(1)	0.006(1)
β_{22}	0.0016(2)	0.000(2)	0.000(1)	0.006(1)
β_{33}	0.0018(2)	0.006(2)	0.005(2)	0.006(1)
β_{12}	0	0	0	0.003(1)
β_{13}	0	0	0	0.003(1)
β_{23}	0	0	0.000(1)	0.003(1)
* Standard deviation is shown in parentheses throughout.				

group. After a few refinement cycles with these positions and anisotropic temperature factors, the reliability factors R = 0.07 for $NaSbO_3$ and 0.08 for $AgSbO_3$ were obtained. The final atomic positions and anisotropic temperature factors for $NaSbO_3$ are shown in Table III-2, and for $AgSbO_3$, in Table III-3. The bond distances in both compounds are shown in Table III-4.

It is interesting to note that the positions of the Na^+ and Ag^+ ions in the Im3 structure can be estimated by calculating the optimum Na-O and Ag-O distances. In $NaSbO_3$, the normalized distance from a Na^+ ion at coordinate (x,x,x) to an O_1^{2-} ion at (0.356,0,0) is

$$D_1/a = [(x - 0.356)^2 + x^2 + x^2]^{1/2} = (3x^2 - 0.712x + 0.1267)^{1/2} \qquad \text{(III-1)}$$

and to an O_2^{2-} ion at (0, 0.334, 0.287) is

$$D_2/a = [x^2 + (x - 0.334)^2 + (x - 0.287)^2]^{1/2} = (3x^2 - 1.242x + 0.1939)^{1/2} \quad \text{(III-2)}$$

where a is the cell constant. If a Na^+ ion is equidistant from its six neighboring oxygen ions, then $D_1 = D_2$ and x = 0.125, as obtained by the structure analysis. Thus, all Na^+ ions are about ideally situated at O_1 -O_2 octahedral sites only. The observed Na-O distances of 2.730 and 2.760 Å, are significantly longer than the sum of the ionic radii of 2.42 Å, which may explain why this phase is difficult to obtain by ordinary methods.

TABLE III-3 ATOMIC POSITIONS AND THERMAL PARAMETERS OF $AgSbO_3$					
Atom Position	Sb 12e	O_1 12d	O_2 24g	Ag_1 16f	Ag_2 16f
Multiplier	1/4	1/4	1/2	$1/3 \times 0.33(3)*$	$1/3 \times 0.44(2)$
X	0.8393(4)	0.371(4)	0	0.111(1)	0.184(1)
Y	0	0	0.296(7)	0.111(1)	0.184(1)
Z	1/2	0	0.291(4)	0.111(1)	0.184(1)
β_{11}	0.0007(4)	0.002(4)	0.009(5)	0.013(2)	0.012(1)
β_{22}	0.0025(5)	0.006(5)	0.05(1)	0.013(2)	0.012(1)
β_{33}	0.0028(5)	0.002(4)	0.008(5)	0.013(2)	0.012(1)
β_{12}	0	0	0	0	0.006(1)
β_{13}	0	0	0	0	0.006(1)
β_{23}	0	0	0.012(9)	0	0.006(1)
* Standard deviation is shown in parentheses throughout.					

TABLE III-4		
BOND DISTANCES (Å) OF $NaSbO_3$ AND $AgSbO_3$		
	$NaSbO_3$	$AgSbO_3$
Octahedron around Sb^{+5}		
$Sb-O_1$ 2×	2.027	1.936
$Sb-O_2$ 2×	1.949	2.279
$Sb-O_2$ 2×	1.996	2.006
Nearest O^{2-} neighbors		
O_1-O_1 1×	2.692	2.421
O_1-O_2 4×	2.864	3.002
O_1-O_2 2×	3.202	2.881
O_1-O_2 2×	2.701	2.828
O_2-O_2 4×	2.774	2.866
Neighbors of Na^+	Neighbors of Ag^+	
$Na-O_1$ 3 × 2.730	Ag_1-O_1 3 × 2.858	
$Na-O_2$ 3 × 2.760	Ag_1-O_2 3 × 2.644	
$Na-Na$ 3 × 2.303	Ag_2-O_1 3 × 3.014	
$Na-Na$ 3 × 3.257	Ag_2-O_2 3 × 2.988	
	Ag_2-O_2 3 × 2.261	
	Ag_1-Ag_1 3 × 2.081	
	Ag_2-Ag_2 3 × 2.154	

The more acidic Ag^+ ions, on the other hand, are located at x = 0.11 and x = 0.20, corresponding to the centers of the O_1-ion and the O_2-ion faces, respectively, as can be seen by minimizing D_1/a and D_2/a with respect to x. The stable SbO_3 network only allows a short Ag-O distance of 2.26 Å, which is intermediate between the covalent bond length (2.05 Å in Ag_2O) and the ionic bond length (2.50 Å in $AgClO_3$). The remaining Ag-O distances of 2.858, 2.644, 2.988 and 3.014 Å are greater than the sum of the ionic radii (2.55 Å).

We can expect the highly ionic ions K^+ and Rb^+ to occupy the O_1-O_2 octahedral sites, as does the Na^+ ion, and the Li^+ to be located at x = 0.20 in order to have the shortest bond distance. Placing the ionic Li^+ ions in octahedral site faces would tend to expand the network relative to the value extrapolated from $RbSbO_3$, $KSbO_3$ and $NaSbO_3$. That a similar expansion is not found in $AgSbO_3$ must be attributed to the tendency of this ion to form covalent bonds.

<div align="right">H. Y-P. Hong</div>

D. STRUCTURE REFINEMENT OF $CuTa_2O_6$, A DISTORTED AND DEFECTIVE PEROVSKITE

To prepare $CuTa_2O_6$, a 4:1 mixture of CuO and Ta_2O_5 was fired in a covered platinum crucible at 1430°C and then cooled at 3.5°/hr for 5 days. The excess CuO used as a flux was then dissolved in concentrated HCl, to yield a black, highly crystalline $CuTa_2O_6$ phase. A single crystal was selected for structural analysis.

Weissenberg photographs and G.E. XRD-5 diffractometer intensities showed diffraction symmetry 3/m with no systematic absence, consistent with space groups P23 and Pm3. The cubic unit cell has the dimension 7.526 Å and contains four $CuTa_2O_6$ molecules. Three dimensional data to $2\theta = 60°$ were collected with Zr-filtered $MoK\alpha$ radiation, using balanced filters and the stationary-crystal, stationary-counter method with 5° take-off angle. Peak heights were counted for 10 sec, and then backgrounds at ±2° of each peak were counted for 10 sec. The intensities were multiplied by Lorentz polarization and ϕ-angle absorption corrections before conversion to structure factors.

Wherever h, k or l are even, the x-ray intensities are much stronger than where they are odd, which implies that the structure is the superlattice of 7.526 Å divided by 2, the normal perovskite cell dimension. Since Ta^{5+} has been found to occur only in octahedral sites in oxides, it was introduced into the 8i positions of space group Pm3. The space group P23 is inappropriate, because it contains only four equivalent positions per unit cell. The 4 Cu atoms per unit cell were initially placed randomly in the sites 3c and 3d, the 24 O atoms in 12j and 12k. After a few cycles of refinement with a least-squares program, a reliability factor R = 0.066 was obtained. The final atomic positions are shown in Table III-5, and the bond distances and angles in Table III-6. (Reinen and Propach[14] have independently deduced the Pm3 space group on the basis of optical and powder-diffraction data, but did not determine the atomic positions.)

The occupancy factors given in Table III-5 for the 3d and 3c Cu sites are 0.80 and 0.48, respectively. The total number of Cu atoms calculated from these factors (2.40 + 1.44 = 3.84) is equal, within experimental error, to the stoichiometric value of 4 per unit cell. Although it is remarkable that so small an ion as Cu^{2+} should occupy the A site of a cubic perovskite, this is made possible by a distortion of the TaO_3 network that reduces the A-site anion coordination from twelve to four nearest neighbors, plus eight next-nearest neighbors. The four nearest neighbors

TABLE III-5

ATOMIC POSITIONS OF CUBIC $CuTo_2O_6$

Space Group: Pm3; a = 7.526Å

Ta in 8i	$\pm(x,x,x;\ x,\bar{x},\bar{x};\ \bar{x},x,\bar{x};\ \bar{x},\bar{x},x)$	$x = 0.2464(2)$*
Cu_1 in 3d	$(1/2,0,0;\ 0,1/2,0;\ 0,0,1/2)$	occupancy factor = 0.80(3)
Cu_2 in 3c	$(0,1/2,1/2;\ 1/2,0,1/2;\ 1/2,1/2,0)$	occupancy factor = 0.48(4)
O_1 in 12k	$\pm(1/2,y,z;\ z,1/2,y;\ y,z,1/2;$ $1/2,y,\bar{z};\ \bar{z},1/2,y;\ y,\bar{z},1/2)$	$y = 0.199(5)$ $z = 0.317(5)$
O_2 in 12j	$\pm(0,y,z;\ z,0,y;\ y,z,0;$ $0,y,\bar{z};\ \bar{z},0,y;\ y,\bar{z},0)$	$y = 0.315(4)$ $z = 0.205(5)$

* Standard deviation is shown in parentheses throughout this column.

TABLE III-6

BOND DISTANCES (Å) AND ANGLES (deg) OF $CuTo_2O_6$

Bond Distonce (Å)	Angle (deg)
Octahedrol around To	O_1-Ta-O_1 $3\times$ 97.8
Ta-O_1 3×1.951	O_1-Ta-O_2 3×172.5
Ta-O_2 3×2.013	O_1-Ta-O_2 $3\times$ 88.3
	O_1-Ta-O_2 $3\times$ 85.4
Rectangular around Cu	O_2-Ta-O_2 $3\times$ 87.9
Cu_1-O_1 4×2.069	Ta-O_1-Ta 143.6
Cu_2-O_2 4×2.036	Ta-O_2-Ta 143.0
	O_1-Cu_1-O_1 $2\times$ 84.7
Oxygen distonce	O_1-Cu_1-O_1 $2\times$ 95.3
O_1-O_1 4×2.941	O_2-Cu_2-O_2 $2\times$ 85.3
1×2.789	O_2-Cu_2-O_2 $2\times$ 94.7
1×3.057	
O_1-O_2 2×2.762	
2×2.690	
O_2-O_2 4×2.795	
1×2.997	
1×2.758	

are coplanar and nearly form a square. The Cu_1-O nearest-neighbor distances are 2.069 Å and the Cu_2-O distances are 2.036 Å, close to the sum of the ionic radii (2.02 Å). The eight next-nearest neighbors are at distances too large for significant Cu-O bonding: 4 Cu_2-O at 2.634Å, 4 Cu_2-O at 3.288Å, 4 Cu_1-O at 2.816Å and 4 Cu_1-O at 3.256Å. The CuO_4 square complexes are isolated from each other, sharing corners with eight TaO_6 octahedra. The TaO_6 octahedra share corners with each other in a zig-zag form having a Ta-O-Ta angle of 143°, instead of the 180° found in the ideal cubic perovskite. The Ta-O distances are very close to those found in $NaTaO_3$, $KTaO_3$ or $AgTaO_3$ perovskites, but the O-Ta-O angles deviate somewhat from 90° and 180°, showing a distorted TaO_6 octahedron.

H. Y-P. Hong

REFERENCES

1. K. J. Planker and E. Kauer, Z. Angew. Phys. 12, 425 (1960); S. Yamada, Y. Kawasaki and O. Nishida, Phys. Stat. Sol. 26, 77 (1968); B. M. Vul, A. F. Plotnikov, V. M. Sal'man, A. A. Sokolova and V. A. Chapnin, Sov. Phys. – Semicond. 2, 1045 (1969); M. P. Lisitsa, V. N. Malinko, E. S. Nikonyuk, N. E. Novoseletskii and G. G. Tsebulya, Sov. Phys. – Semicond. 3, 1321 (1970).

2. W. P. Dumke, M. R. Lorenz and G. D. Pettit, Phys. Rev. B1, 4668 (1970).

3. A. Onton, Y. Yacoby and R. J. Chicotka, Phys. Rev. Letters 28, 966 (1972).

4. G. W. Iseler, J. A. Kafalas, A. J. Strauss, H. F. MacMillan and R. H. Bube, Solid State Commun. 10, 619 (1972).

5. Solid State Research Report, Lincoln Laboratory, M. I. T. (1971:4), p. 44, DDC AD-736501; (1972:1), p. 33, DDC AD-740874.

6. J. L. Sommerdijk, J. Luminescence 4, 441 (1971).

7. T. Kano, H. Yamamoto and Y. Otomo, J. Electrochem. Soc. 119, 85C (1972).

8. R. E. Thoma, G. M. Hebert, H. Insley and C. F. Weaver, Inorg. Chem. 2, 1005 (1963).

9. F. Hund, Z. Anorg. Allgem. Chem. 261, 106 (1950).

10. P. Spiegelberg, Arkiv. Kemi 14A, No. 5, 1 (1940).

11. N. Morrow and L. Katz, 1967 Mtg. Am. Crystallog. Assoc., paper R-6.

12. J. M. Longo and A. W. Sleight, Inorg. Chem. 7, 108 (1968), DDC AD-668730.

13. Solid State Research Report, Lincoln Laboratory, M. I. T. (1971:4), p. 35, DDC AD-736501.

14. D. Reinen and V. Propach, Inorg. Nucl. Chem. Letters 7, 569 (1971).

IV. PHYSICS OF SOLIDS

A. RARE-EARTH PHOSPHORS FOR NEAR-INFRARED-TO-VISIBLE UPCONVERSION

We are continuing our study of near-infrared excitation of phosphors to achieve visible radiation in the system $NaYF_4:Yb^{3+}, Er^{3+}$. The primary emphasis has been to achieve the highest effective excitation, in order to determine the level at which saturation effects limit the efficiency.

Although there is continuing difficulty in producing a sample of a given composition with the same luminescing properties from run to run, in the last quarter a sample has been made with composition $NaY_{0.8}Yb_{0.18}Er_{0.02}F_4$ which is approximately twice as effective in producing green luminescence for a given infrared excitation as the sample discussed in the preceding Solid State Research Report.[1] All measurements reported here were made on this new sample.

Our excitation sources included a xenon arc lamp operating at 20 A CW, or at 130 A pulsed for 15 msec with a repetition rate of 1 sec. This source was focused on the sample through a Baird-Atomic 9750-Å filter with a 150-Å half-band width. In addition, to achieve higher effective inputs, a Nd-YAG laser was employed. Although the laser was CW, it was mechanically chopped to have the beam strike the sample with a 20-msec pulse width at a 1-sec pulse rate. This was necessary to reduce the heating effect of the laser beam. The visible emission goes through a monochromator to a photomultiplier tube and finally to a Keithley boxcar integrator, which was gated to read the output signal just before the end of the pulse.

The resulting variation of visible emission as a function of infrared excitation is shown in Fig. IV-1. Since the Nd-YAG laser wavelength badly mismatches the excitation spectrum of the phosphor, the effective laser input intensity relative to the true input of the xenon source optical system was obtained by matching the green/red/blue output ratios. This technique has previously been employed by Rich and Pinnow.[2]

Taking the exponential relationship $O = I^n$, where O = visible emission and I = infrared excitation intensity, $n = 2$ for the lower values of I in Fig. IV-1. For blue emission, $n = 3$ at input levels to the left of the lowest point shown on the blue emission curve. At input levels approximately corresponding to this point, an observable change in slope occurs in all the emission curves. While these changes involve a reduction in the value of n for green and blue emission, n increases to approximately 2.25 for red emission. This higher value is indicated by the heavy dashed line of Fig. IV-1.

This increase in n is significant, since it establishes that the mechanism of upconversion is itself a function of the infrared excitation intensity level. In particular, Sommerdijk,[3] in his study of the mechanism of red upconversion of $NaY_{0.77}Yb_{0.20}Er_{0.03}F_4$, eliminated the three-step process as a factor because he found $n = 2$. It is now apparent that this is true only at the lower input levels. An intense source changes the distribution of upconversion mechanisms so that the three-step process represents a significant proportion of red emission.

A further indication of a change in upconversion processes is our observation that at the more intense input levels the time required for the visible emission to reach a constant value
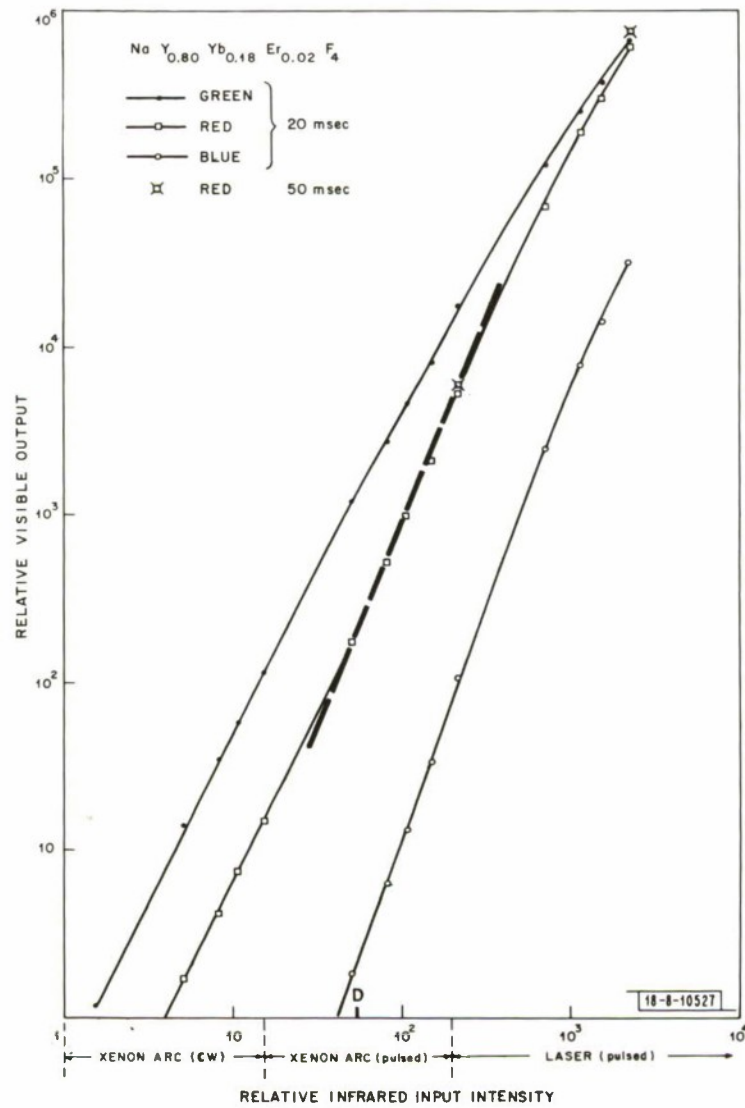
Fig. IV-1. Variation of visible light emission with infrared excitation intensity. D is effective input position.

increased with increasing excitation. Over the region of laser excitation, this rise time exceeded 20 msec, so the points in this region shown in Fig. IV-1 lie below the true steady-state output. This effect is greatest for the red emission. Measurements using 50-msec pulses yielded the two points included in Fig. IV-1 for comparison with the 20-msec data; the highest point had still not achieved a steady-state value.

The radiant efficiency of infrared-to-visible luminescence in our sample, in the optical system described above, is shown in Fig. IV-2. It is based on comparison of luminescence with diffuse reflection from MgO in each of the spectral regions in which luminescence occurs. A total

Fig. IV-2. Efficiency of visible light emission in optical system as a function of infrared excitation intensity.
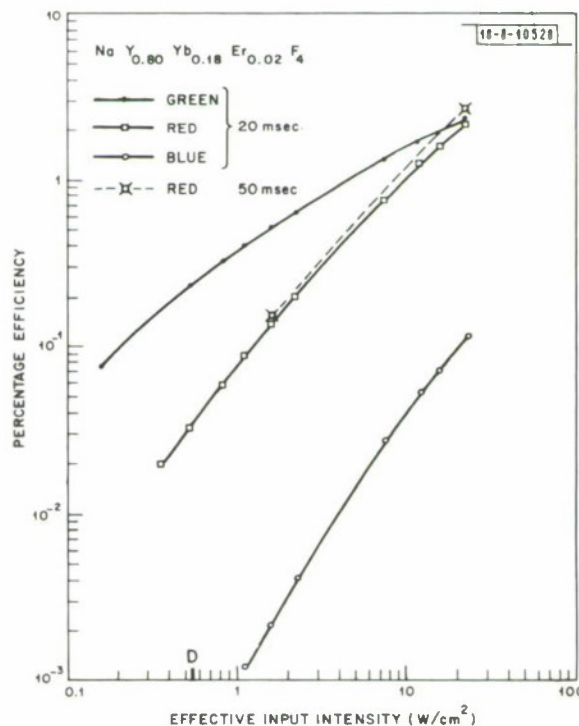
radiant efficiency of over 5 percent is achieved at an effective input intensity of 22 W/cm^2, and the efficiency is still rising at a significant rate with increasing excitation. Since this represents an excitation level well beyond that which is presently available on a CW basis in this spectral region, it appears that saturation effects do not represent the primary limitation in the system $\text{NaYF}_4 : \text{Yb}^{3+}, \text{Er}^{3+}$.

The primary problem lies with the infrared excitation source and the interface between it and the phosphor. The most practical source to date has been a GaAs:Si diode. A Texas Instruments, T1XL12 diode with a 17 percent efficiency, coated with a slurry of our sample and glycerine, yielded a green/red/blue output ratio corresponding to the effective input position labeled D in Fig. IV-2. The slurry consisted of particles of differing size, at varying distance from the diode surface. Hence they were subjected to differing excitation levels. In addition, there is the problem of reflection back into the diode, as well as the appearance of a significant amount of infrared excitation which passed through the slurry unaffected (in addition to the infrared
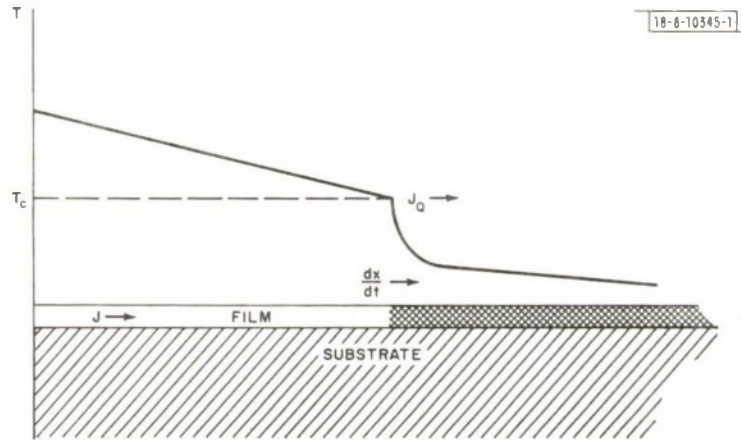
Fig. IV-3(o). Schematic diagram showing motion of o phase boundary in the presence of on electric current of density J ond heat flow J_Q.
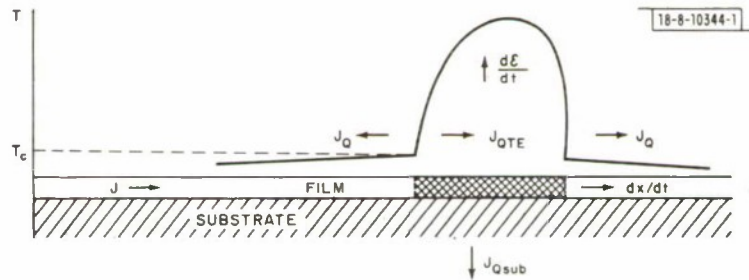
Fig. IV-3(b). Schematic representation of the steady stote motion of o pulse of insuloting phose injected into the metallic phose in the presence of electric current. J is electric current density; J_Q, heat flow; J_{QTE}, thermoelectric heat flow; $J_{Q\,sub}$, heot flow to the substrote; $d\mathcal{E}/dt$, Joule heat input; ond T_c, tronsition temperoture.

excitation emitted at slightly longer wavelength). Therefore, an uncertainty factor of 2 on the position of D appears reasonable.[2]

N. Menyuk
K. Dwight
J. W. Pierce

B. METAL-INSULATOR TRANSITION

The free energy description of the metal-insulator transition, developed earlier for the case of Ti_2O_3 with one electron per titanium ion, has been modified to cover the case of V_2O_3 with two electrons per vanadium ion.[4] The new model is being programmed and will be studied for indications of a phase transition in V_2O_3.

Equations describing the motion of the boundary between insulator and metal phases in the presence of an electric current have been obtained [see Figs. IV-3(a and b)]. We considered a one-dimensional problem, with the heat flow in either phase described by a partial differential equation of the form

$$\frac{\vec{J}^2}{\sigma} + \kappa\nabla^2 T - \mathcal{I}\vec{J}\cdot\nabla T - c_A(T - T_A) = c\,\frac{\partial T}{\partial t} \quad . \tag{IV-1}$$

In Eq. (IV-1), the first term is the Joule heat input; the second represents heat flow; the third, thermoelectric heat flow; the fourth, heat flow to the ambient or the substrate; and the right-hand side, the rate of increase of energy per unit volume. $\vec{J}$ is the constant current density flowing; σ, electrical conductivity; κ, thermal conductivity; $\mathcal{I}$, Thompson coefficient; c_A, a constant; T_A, ambient temperature; and c, specific heat of the material. The motion of the phase boundary is determined by the boundary condition,

$$[-\kappa_2\nabla T_2 + \epsilon_2 T_c J] - [-\kappa_1\nabla T_1 + \epsilon_1 T_c J] = -[u_1 - u_2]\,\frac{dx}{dt} \quad , \tag{IV-2}$$

where 2 and 1 refer to conditions on two sides of the phase boundary; and ϵ is the thermoelectric power; T_c, critical temperature for the transition; dx/dt, velocity of the phase boundary; and $(u_1 - u_2)$, difference in internal energies per unit volume between the two phases. Equations (IV-1) and (IV-2) are sufficient to determine the motion of the domain boundary.

In general, solution of the problem is very difficult. However, a steady-state solution can be obtained for the propagation of a pulse of insulating phase injected into an infinite strip of conducting phase [see Figs. IV-3(a and b)]. This problem is now being programmed and will be studied as a function of the different parameters of the system.

H. J. Zeiger

C. LASER SPECTROSCOPY

1. Magnetic Resonance of NO with a CO Laser

The fundamental vibration-rotation band of NO centered at 5.3 μm heavily overlaps the wavelength region (5.2 to 6.5 μm) in which the CO laser operates. While there are a few near coincidences between NO absorption lines and the CO laser lines,[5] none of the CO laser lines lie within the low pressure Doppler width of a nitric oxide line. We have used Zeeman tuning of several absorption lines of the paramagnetic NO gas to bring them into exact coincidence with CO laser lines. In this manner we have obtained resolved absorption spectra of NO with the fixed frequency CO laser.

The measurements were made using either a high stability alcohol-cooled (−80°C) $CO-N_2-He-Xe$ laser[6] or a low stability liquid-nitrogen-cooled $CO-N_2-He-Air$ laser. The frequency stability of these lasers determines our effective resolution; the estimated short term instabilities are $\lesssim 0.1$ MHz (Ref. 6) and $\lesssim 10$ MHz, respectively. Both lasers were operated with small intracavity apertures to insure single-mode operation, and with a diffraction grating as one cavity mirror for discrete frequency tuning. The NO gas was contained in a cell of 4 cm length which was placed in the room temperature bore of a 50-kG superconducting solenoid. The linearly polarized laser radiation was propagated along the DC magnetic field, which was homogeneous to ±2 percent over the cell length. After traversing the gas cell, the laser beam was attenuated, passed through a grating spectrometer for absolute calibration purposes, and monitored with a room temperature pyroelectric detector.

The $P(13)_{9,8}$ CO laser line has a calculated frequency of 1884.357 ± 0.006 cm^{-1} (Ref. 7), while the $R(3/2)_{3/2}$ line of NO is at 1884.318 ± 0.004 cm^{-1} (Ref. 8). The separation of 0.039 cm^{-1} for these two lines is small and the g-factor for the $J = 3/2$ energy level in the $^2\Pi_{3/2}$ electronic state is relatively large, $g(3/2) \approx 0.78$. Thus, one needs only a few kG to bring the $R(3/2)_{3/2}$ line into coincidence with the $P(13)_{9,8}$ CO laser line. Figure IV-4 shows the signal transmitted through the gas cell (20-torr NO) as a function of magnetic field. The high stability CO laser was used
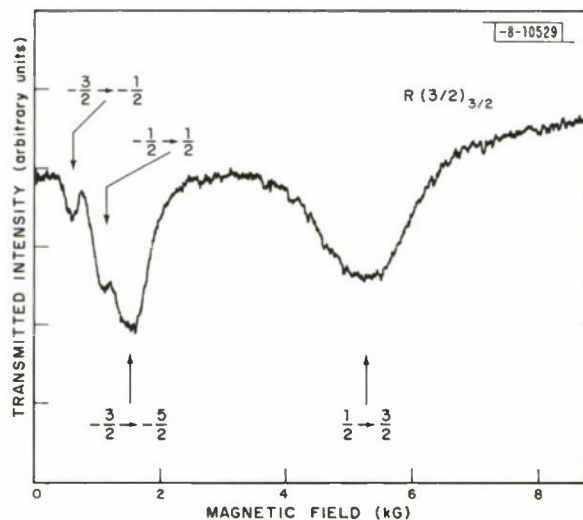
Fig. IV-4. Intensity of CO laser radiation [$P(13)_{9,8}$ line] transmitted through 4 cm of NO at 20 torr vs magnetic field.

while operating on the $P(13)_{9,8}$ line. There are four absorption lines immediately apparent. These four lines comprise one-half of the eight line Zeeman pattern for the $R(3/2)_{3/2}$ transition. The radiation is polarized perpendicular to the field and the electric dipole selection rule is $\Delta M_J = \pm 1$, leading to eight possible lines for this $J = 3/2$ to $J = 5/2$ transition. Since the $P(13)_{9,8}$ CO laser line lies above the $R(3/2)_{3/2}$ zero-field frequency, we observe only the four lines of the Zeeman pattern which have increasing frequency as the field is increased. These transitions are identified in Fig. IV-4 by the initial and final values of M_J. The theoretical relative intensities of these lines for a symmetric top molecule are (left to right) 2, 6, 12 and 24, in good qualitative agreement with the data of Fig. IV-4. From the measured line positions and the theoretical g-factors, we find the separation of the $R(3/2)_{3/2}$ NO line and the $P(13)_{9,8}$ CO line to be about 0.028 cm^{-1}, somewhat smaller than the calculated value of 0.039 cm^{-1}.

There are at least half a dozen other NO absorption lines which fall near enough to CO laser lines to be magnetically tuned for resonance spectroscopy. We have taken preliminary data on $R(3/2)_{1/2}$, $Q(3/2)_{3/2}$ and $Q(5/2)_{3/2}$. A more detailed study of these and other lines is planned.

F. A. Blum
K. W. Nill

2. Isotope Shift in the Fundamental Band of CO: Spectroscopic Determination of the Isotopic Mass of C^{13}

Using a $PbS_{0.82}Se_{0.18}$ diode laser operating near 4.7 μm, we have extended our previous[9] high resolution measurements on $C^{12}O^{16}$ to a study of the $C^{13}O^{16}$ isotope. From a precise measurement of the spacing between absorption lines of the two CO isotopes, we have deduced a value for the ratio of the reduced mass of $C^{12}O^{16}$ and $C^{13}O^{16}$ in good agreement with the accepted mass spectrographic value.

The isotopic mass of C^{13} has previously been determined from infrared spectroscopic data by fitting the measured location of numerous vibration-rotation lines of $C^{13}O^{16}$ to a theoretical model having the C^{13} mass as a parameter.[10] This procedure yields a fairly accurate mass value from data obtained with a spectrometer having a resolution of only 0.1 to 0.2 cm^{-1}. Using an alternative spectroscopic technique, we have determined the ratio of the reduced masses of the two isotopes from a precise measurement (±0.0015 cm^{-1}) of the spacing between an absorption line of each of the isotopes. The two lines studied were the P(4) line of $C^{12}O^{16}$ and the R(8) line of $C^{13}O^{16}$. These lines lie near 2127.68 cm^{-1} and have a measured separation of 0.015 cm^{-1} ± 0.0015 cm^{-1}. The wavelength of the laser was grossly tuned about 20 cm^{-1}, using a magnetic field of 34 kG to obtain coincidence of the laser mode and the absorption lines. The separation between the absorption lines was obtained by current tuning a laser mode through the absorption line. The CO gas used in these measurements was not isotope-enriched, and pressures up to 3 torr in a 10-cm cell were required to obtain the desired absorption spectra on the less abundant (~1 percent) $C^{13}O^{16}$ isotope. The value obtained for the reduced mass ratio of $C^{12}O^{16}$ to $C^{13}O^{16}$ was 0.9559120. This value may be compared with values obtained using the conventional spectroscopic analysis of several lines, 0.9558991 (Ref. 11), and the accepted value obtained from mass spectrographic analysis, 0.9559132 (Ref. 12). We have not yet determined the errors involved in our analysis, such as those associated with the ±0.0015 cm^{-1} uncertainty in the line spacing. However, the excellent agreement between our determination and the accepted value suggests that this procedure may prove to be a useful technique for spectroscopic determination of isotopic mass ratios.

Data were also obtained on two widely spaced isotopic lines, P(5) of $C^{12}O^{16}$ and R(7) of $C^{13}O^{16}$. Figure IV-5 shows these lines and indicates the measured spacing of 0.55 ± 0.06 cm^{-1}. The absorptions shown in Fig. IV-5 were produced by two separate laser modes. Mode 1 is swept through the R(7), $C^{13}O^{16}$ absorption at very nearly the same current that Mode 2 sweeps through P(5) of $C^{12}O^{16}$. Since the largest inaccuracy in our measurements is the laser tuning rate, the large line separation of 0.55 cm^{-1} results in a large uncertainty (±10 percent). The calculated spacing [10] of these lines (0.588 cm^{-1}) lies within the error limits of our measurement (0.55 ± 0.06 cm^{-1}).

K. W. Nill
F. A. Blum
T. C. Harman
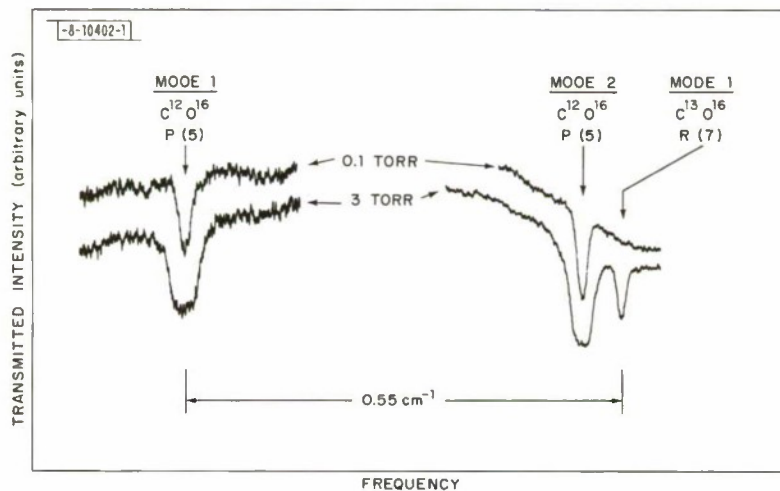
Fig. IV-5. Absorption lines of $C^{12}O^{16}$ ond $C^{13}O^{16}$ isotopes obtoined using two modes of o $PbS_{0.82}Se_{0.18}$ laser. Tuning of Mode 1 indicotes o 0.55 cm^{-1} spacing between P(5) of $C^{12}O^{16}$ ond R(7) of $C^{13}O^{16}$.

TABLE IV-1			
OPTICALLY PUMPED, FAR-INFRARED LASER LINES FROM NH_3			
Pump		For-Infrored Rodiotion	
Wovelength (μm)	Tronsition	Wovelength (μm)	Transition
10.333	R8	282.1	Q(2,2) J = 2 → 2
10.350	R6	291.2	Q(5,4) J = 5 → 5
		72.6	Q(5,4) J = 5 → 4
10.365	R4	58.0	Q(7,5) J = 7 → 6
10.719	P32	151.9	Q(5,3) J = 5 → 4

3. Application of Optically Pumped, Submillimeter Lasers to GaAs Linewidth Studies

Numerous new submillimeter laser lines have been generated using TEA CO_2 lasers to optically pump molecular systems (Ref. 1, p. 42). In our most recent work, population inversion and oscillation have been obtained from both the rotational and inversion-split states of NH_3. These new transitions, identified and listed in Table IV-1, are stable and well suited for spectroscopic applications.

One particular problem of interest is the linewidth of hydrogenic donor transitions in GaAs.[13] Theory indicates that the major contributions to the observed widths come from interactions with the electric fields from surrounding charged donors and acceptors. These interactions, when expanded in Taylor series, are dominated by second-order, Stark perturbation terms and terms involving the donor's quadrupole moment. This moment for the 2p, m = −1 state goes through zero at approximately 55 kG.

Using the Zeeman effect on the donor states, the 1s → 2p, m = −1 transition in GaAs can be tuned through a 291.2-μm laser line by varying the field, as shown in Fig. IV-6. The contribution to the linewidth at this field (55 kG) is almost entirely due to the quadratic Stark effect, which yields a strongly asymmetric lineshape. Comparing this data with that obtained from the 1s → 2p, m = 0 transition and CW, optically pumped lasers at 190 μm, information can be obtained on the number and distribution of impurities.

At the moment, our experimental results indicate only order-of-magnitude agreement with theoretical predictions based on the number of donors and acceptors measured electrically.
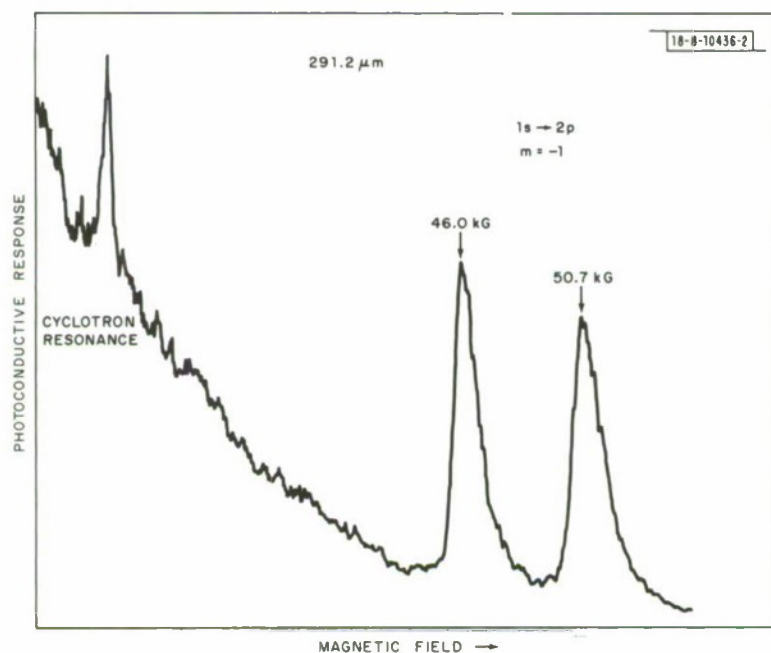
Fig. IV-6. Variotion in GoAs of photoconductive response with mognetic field at 291.2 μm ond T = 4.2°K. Indicoted on trace ore cyclotron resonance ond Zeeman splitting of donor states.
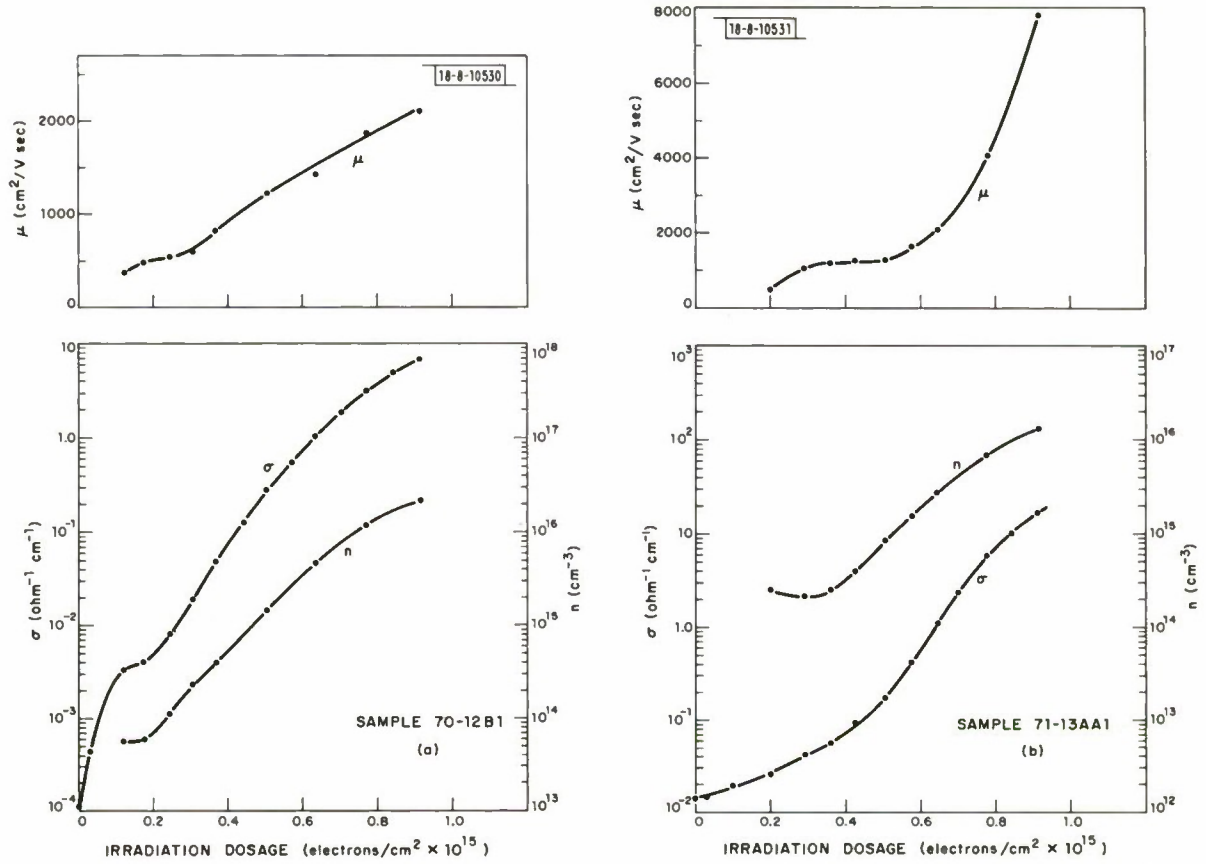
Fig. IV-7. Increase of conductivity, electron density and mobility as a function of electron irradiation (number of electrons per cm^2) for samples (a) 70-12B1 and (b) 71-13AA1. All measurements were made at 8°K.

Further work is in progress. It must be noted that our measurements required attenuating the submillimeter 291.2-μm radiation by a factor of fifty to avoid power broadening. This indicates that the high peak power of these pumped submillimeter systems has interesting nonlinear possibilities.

H. R. Fetterman   D. M. Larsen
J. Waldman   C. M. Wolfe
C. D. Parker

D. IMPERFECTIONS IN SEMICONDUCTORS

1. Electron Irradiation Damage and Annealing of $Hg_{1-x}Cd_xTe$ at Low Temperatures

Samples of $Hg_{1-x}Cd_xTe$ with x = 0.22 and x = 0.31 have been irradiated with dosages of up to $1 \times 10^{15}/cm^2$ of 2.5 MeV electrons. The samples were mounted on the cold finger of a helium dewar and during irradiation remained at a temperature below 25°K. The irradiation changed initially p-type samples* to n-type, producing up to 10^{16} electrons/cm^3 at 8°K. Figures IV-7(a, b) show the dependence of conductivity, electron concentration and mobility on electron irradiation dosage.

After irradiation, the samples were annealed by heating for 15 minutes at progressively higher temperatures and returning to 8°K after each step to make the measurements. Figures IV-8(a, b) show the conductivity, carrier concentration and mobility as a function of annealing temperature. In both samples, much of the change in electrical properties due to annealing occurs between 50° and 75°K. This low temperature annealing is thought to be due to lattice defects rather than trap effects, since it could not be induced by illuminating the sample with intense light.

Photoluminescence and photovoltaic response were also measured before and after irradiation and at several stages of the annealing. As seen on the left in Fig. IV-9, for sample 70-12B1[†] irradiation broadens the emission spectrum obtained by exciting the sample with a GaAs diode laser mounted in the dewar tail and shifts it toward longer wavelengths. Whereas annealing to 106°K decreases the electron concentration of the samples by two orders of magnitude, the luminescence spectrum seems to show little change. Most of the effect of electron irradiation on the luminescence anneals out between 106° and 231°K. The spectrum observed after annealing at room temperature is shifted slightly toward shorter wavelengths from the pre-irradiation spectrum. In fact, the helium temperature conductivity of the sample at this point is still a factor-of-25 higher than the initial conductivity, and a hole concentration of $4.5 \times 10^{14}/cm^3$ is obtained by the relation R = 1/pe.

The photovoltaic response of the sample is shown on the right in Fig. IV-9. The effect of irradiation is seen to greatly broaden the cutoff and to shift it toward longer wavelengths. A photoconductive signal with the same spectral response was also observed. However, when the current was limited to the ohmic region, the photoconductive signal was smaller than the photovoltaic signal.

Proton irradiation at room temperature[15] converts p-type $Hg_{1-x}Cd_xTe$ to n-type for compositions 0.25 < x < 0.5. However, irradiation of samples with x ≃ 0.2 failed to produce n-type material.[16] In contrast, our results indicate that low temperature electron irradiation converts p-type to n-type material for compositions x = 0.31 and x = 0.22.

---

* The samples had approximately 3×10^{16} holes/cm^3 at 77°K. At 8°K they had low conductivity, and the Hall constant could not be measured.

† The transport properties of sample 70-12B1 have been studied in detail.[14]
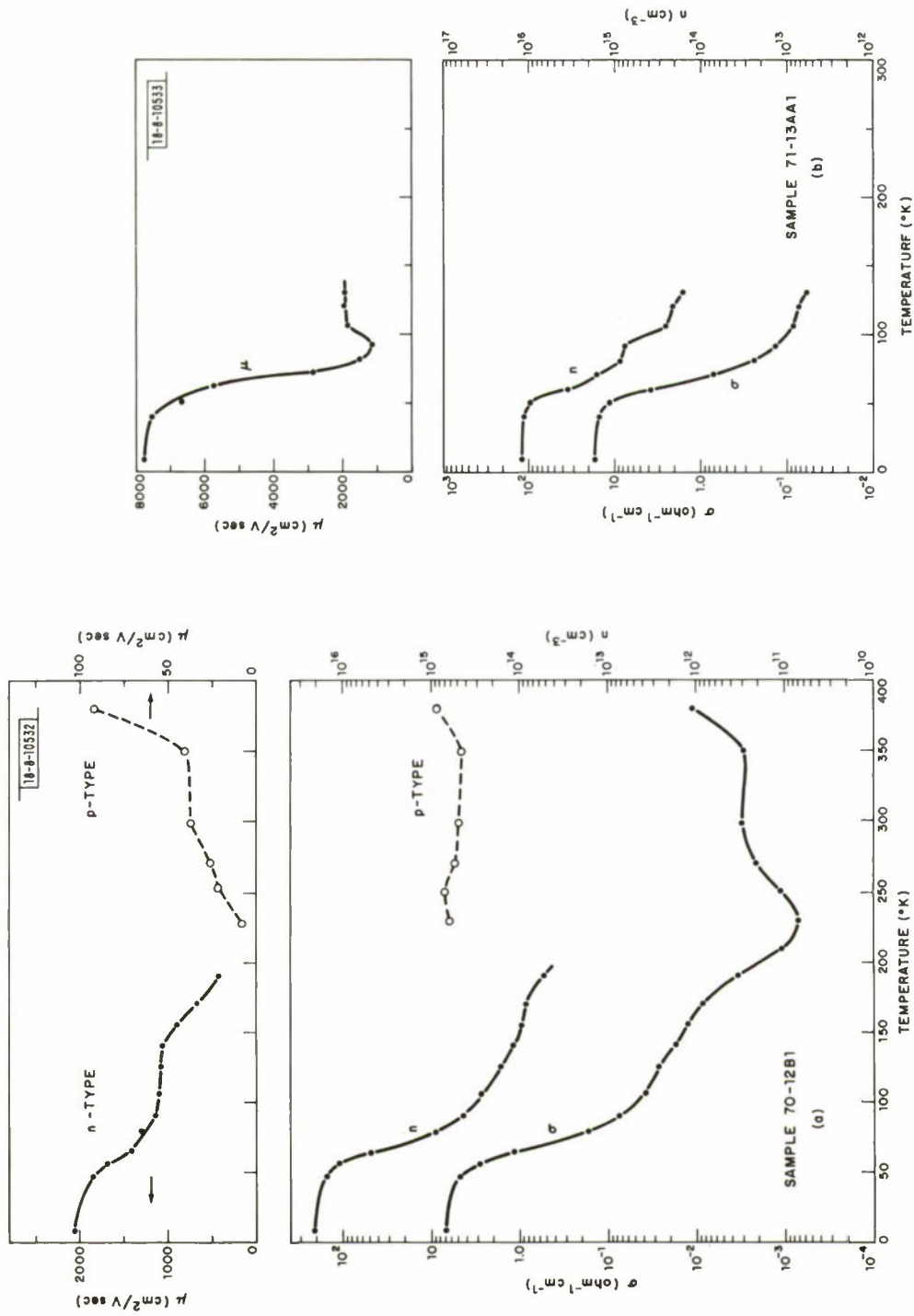
Fig. IV-8. Conductivity, carrier concentration and mobility at 8°K as a function of annealing temperature for samples (a) 70-12B1 and (b) 71-13AA1. Samples were held at each successively higher annealing temperature for 15 minutes, then returned to 8°K for measurement.
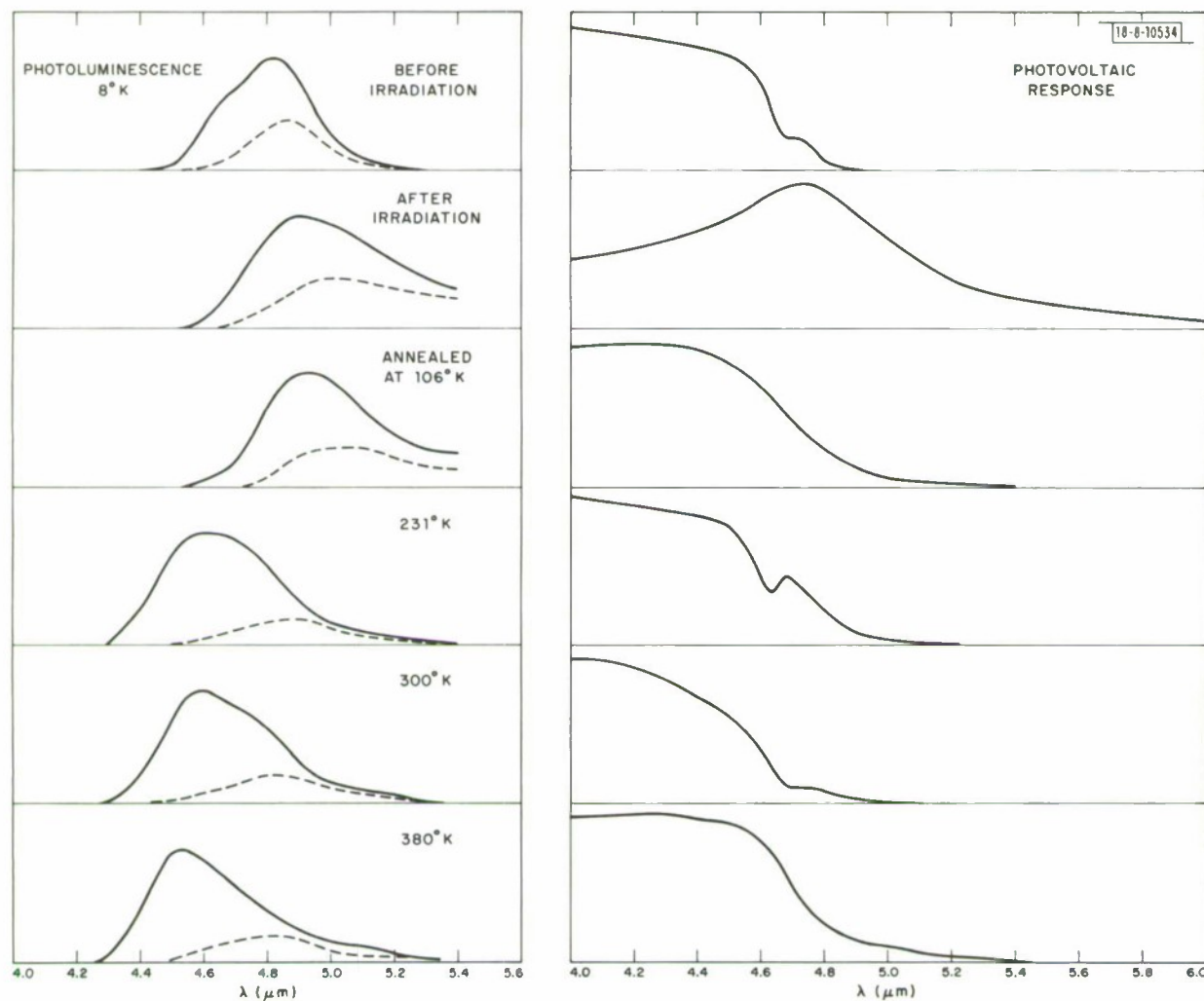
Fig. IV-9. On left: photoluminescence spectrum of sample 70-12B1 at various stages. Dashed line in each case is obtained with GaAs exciting laser power decreased to 1/4. Laser powers used are the same in all cases. Vertical scales are arbitrary except that they are the same for both full and reduced power curves in each case. InSb detector cuts off at 5.4 μm. Curves have been corrected for decreasing detector response between 5.1 and 5.4 μm. Peak signal to noise was 5, and resolution was 0.1 μm in the worst case. On right: photovoltaic response of sample 70-12B1 at various stages. Vertical scales are arbitrary. Post-irradiation response was about a factor-of-10 weaker than pre-irradiation response, and became stronger with annealing. Dips in some of the curves seen at 4.6 to 4.7 μm are due to a competing signal of opposite polarity. Focusing incident light on a different spot can deepen the dip or reverse polarity of the signal.

The shifts of the luminescence and photovoltaic cutoff toward lower energy indicate that low temperature electron irradiation introduces energy levels into the forbidden gap. Displacement threshold studies[17] may help to identify the defect species produced.

J. Melngailis   W. C. Kernan
J. L. Ryan*   H. Rosen*
T. C. Harman

2.   Effect of Lattice Vacancies on Electrical Resistivity of Small Gap Semiconductors

A previous investigation[18] of the band structure of $Pb_{1-x}Sn_xSe$ alloys for compositions $x = 0.17$ and 0.20 (i.e., near zero gap) revealed the surprising result that the value of pressure at the resistivity minimum, which is expected to occur near where the energy gap goes through zero, depends on carrier concentration and also carrier type. In an attempt to understand this phenomenon, we are studying a theoretical model of the effect of lattice vacancies on the electrical resistance of a compound semiconductor, based on a T-matrix formalism.[19] The self-energy of a band electron in the presence of vacancies is formally calculated. Self-energy is expressed in terms of matrix elements of the vacancy perturbation potential, evaluated with respect to Kohn-Luttinger basis states. The results are applied to a simplified model of a compound semiconductor, assuming only a few bands are important in the evaluation of self-energy. Electrical resistance is then calculated, based on a phenomenological Boltzmann transport theory.

R. W. Davies
H. J. Zeiger

---

* Group 69.

REFERENCES

1. Solid State Research Report, Lincoln Laboratory, M.I.T. (1972:1), p. 33, DDC AD-740874.

2. T.C. Rich and D.A. Pinnow (to be published).

3. J.L. Sommerdijk, J. Luminescence 4, 441 (1971).

4. H.J. Zeiger, T.A. Kaplan and P.M. Raccah, Phys. Rev. Letters 26, 1328 (1971), DDC AD-729576; Solid State Research Report, Lincoln Laboratory, M.I.T. (1971:4), p. 48, DDC AD-736501.

5. R.T. Menzies, N. George and M.L. Bhaumik, IEEE J. Quant. Electron. QE-6, 800 (1970).

6. C. Freed, Appl. Phys. Letters 18, 458 (1971), DDC AD-729613.

7. A.W. Mantz, E.R. Nichols, B.D. Alpert and K.N. Rao, J. Mol. Spectry. 35, 325 (1970).

8. D.B. Keck and C.D. Hause, J. Mol. Spectry. 26, 163 (1968); J. Chem. Phys. 49, 3458 (1968).

9. K.W. Nill, F.A. Blum, A.R. Calawa and T.C. Harman, Appl. Phys. Letters 19, 79 (1971), DDC AD-734114.

10. W.S. Benedict, R. Herman, G.E. Moore and S. Silverman, Astrophys. J. 135, 277 (1962).

11. E.K. Plyler, L.R. Blaine and E.D. Tidwell, J. Research NBS 55, 183 (1955).

12. W.F. Hornyok, T. Lauritsen, P. Morrison and W.A. Fowler, Revs. Mod. Phys. 22, 291 (1950).

13. D.M. Larsen, Bull. Am. Phys. Soc. 17, 369 (1972).

14. C.T. Elliot, I. Melngailis, T.C. Harman and A.G. Foyt, J. Phys. Chem. Solids (to be published).

15. A.G. Foyt, T.C. Harman and J.P. Donnelly, Appl. Phys. Letters 18, 321 (1971), DDC AD-729605.

16. A.G. Foyt, personal communication.

17. F.J. Bryant, A.F.J. Cox and E. Webster, J. Physics (C) 1, 1737 (1968).

18. Solid State Research Report, Lincoln Laboratory, M.I.T. (1971:4), p. 57, DDC AD-736501.

19. R.W. Davies, Ph.D. Thesis, Carnegie Institute of Technology, 1964 (unpublished).

V. MICROELECTRONICS

A. MASK-MAKING LABORATORY

Recent efforts in the mask-making laboratory are concentrated in the following areas:

(1) Reducing defect density.

(2) Finding a reliable vendor for chrome photoplates.

(3) Developing image test targets.

Efforts to reduce pinholing and other defects are continuing to improve the quality of our work. Most recent efforts are directed toward pinholes in the chrome masks. We discovered that more than half of these defects can be traced to the quality of the chrome and its photosensitive coating. In order to help us get high quality chrome blanks, we wrote a set of specifications for the glass, chrome and photoresist. Since we now check incoming chrome blanks against these specifications, improved yields have resulted.

We undertook an extensive effort to find a reliable source for high quality chrome blanks. The reasons for this task are:

(1) It will relieve our thin film laboratory from the routine task of preparing such plates.

(2) It will make it unnecessary for us to develop quality control procedures for uncoated glass plates.

(3) It is hoped that a commercial supplier will provide a product of consistent high quality.

In efforts to find an outside supplier of 0.250-inch-thick glass chrome plates, we found that glass of this thickness with a surface finish adequate for microelectronics masks is extremely difficult to obtain. We therefore conferred with the people for whom we were making these thick masks in order to ascertain whether or not they could use thinner plates. With this slight stimulus, they designed a vacuum contact-printing fixture which works better with 0.060-inch-thick masks than their old pressure jig did with the 0.250-inch-thick masks.

This new development made our chrome plate procurement problem much simpler, since 0.060-inch-thick chrome plates are becoming an industry standard. We have used 0.060-inch-thick Bell and Howell plates for some time for less critical work. We are awaiting a quotation from them for plates selected to our specifications.

In the meantime, we are looking for other sources for these plates, and we have found two additional suppliers who can meet our specifications. Unfortunately, the highest quality plates are not supplied with a photoresist coating, as are the others. As an example of the stringency of our specifications, one major mask manufacturer who wants to make chrome blanks for us is unable to meet our specification of no pinholes larger than $0.5\,\mu m$ in the blank chrome plate.

Although we successfully reproduce $1.3\text{-}\mu m$ lines on a routine basis, we have been unable to reproduce $1.0\text{-}\mu m$ lines on chrome. However, we have resolved such lines on emulsion. In an effort to improve our limiting resolution on chrome, we prepared a resolution test chart which can be used to study the properties of our lens and the effects of different processing procedures.

D. L. Smythe, Jr.

B. SEMICONDUCTOR DEVICES AREA

1. Electron Beam Semiconductor (EBS) Diodes

The n on p semiconductor diodes being produced for the EBS program meet required electrical specifications for leakage, punch-through, thermal resistance and minimum voltage breakdown. However, the shield arrangement to protect the oxide from the electron beam is not entirely satisfactory, either because of thin spots in the gold shield or because of voids occurring at the bonded interface, either between the shield and the package or between the shield and the device. The attachment of the shield is troublesome because of the large diameter bond required and the relatively poor surface common to the present packages. Thicker shields are being prepared in an alternative fashion which may reduce the problem of thin spots, although they may aggravate the bonding problems. Other approaches to prevent the electron beam from creating an oxide charge are also being pursued. These include different oxides and glass passivation, as well as heavy epoxy coatings. Evidence of contamination on some diodes after operation in the Group 91 system suggests that diode degradation may result from the operational environment, even after the oxide charge problem is solved.

Some disagreement exists regarding the actual value for the thermal resistance of the present packaged devices. Our measurements indicate typical values of $1°\,C/W$, or less, and independent measurements of these devices by commercial organizations correlate well with our findings. However, a theoretical analysis by Group 91 personnel of thermal resistance for the EBS devices and package indicates that no less than $1.8°\,C/W$ is possible. In any case, the original requirement for a thermal resistance of less than $3°\,C/W$ has been achieved.

Additional EBS units selected from the groups of delivered units are operated in an elevated temperature-bias environment to evaluate their long-term stability. No failures have occurred in 1000 hours of testing.

2. Optoelectronics Program

Several experiments on wafer processing with different doping are in progress for the optoelectronics sensor program. The structural and fabrication problems related to the large diameter devices and their immersion in liquid He seems to have been resolved. The current effort is primarily directed toward understanding the variations which exist in the finished units and toward further processing with different dopants.

The partially completed epitaxial reactor system is being used with good results to produce silicon nitride passivation for silicon devices. Initial use of silicon nitride is being made for further work in the SIMTOP process.

R. A. Cohen

C. DEPOSITION OF METAL OXIDE THIN FILMS BY RF REACTIVE SPUTTERING

A program is under way in cooperation with Group 83 (Electronic Materials) to prepare high quality thin films of the oxides of certain metals and metal alloys. Of particular interest are crystalline VO_2 (one of the many oxides in the vanadium-oxygen system), amorphous SnO_2, and mixtures of SnO_2 and Sb_2O_5. Information in the literature and early experiments indicated that none of these films could be prepared by sputtering onto an unheated substrate. Since the design

of the substrate platform in the sputtering equipment available for this work precluded the incorporation of direct heating, a copper block heated by six cartridge heaters was designed which would sit on the substrate platform (separated from the aluminum of the platform by thin, ceramic spacers). This block is capable of heating substrates uniformly to temperatures in excess of 600°C. However, because of space limitations within the vacuum chamber, no cooling is available to the heated block and the resultant cool-down period of several hours limits the number of runs that can be made to one per day.

Very thin films (less than 200Å) of high quality, amorphous SnO_2 and SnO_2/Sb_2O_5 mixtures have been prepared by RF reactively sputtering either pure Sn or a Sn/Sb alloy in a mixture of between 5 and 20 percent O_2 in Ar. The total pressure of the sputtering gas is between 5 and 10 mtorr, and the substrate temperature is maintained at temperatures close to 600°C. Films of pure VO_2 have not yet been obtained. However, films of mixed oxides which are predominately VO_2 have been prepared, and show very promising electrical properties. These films are prepared by sputtering in a gas mixture of between 10 and 15 percent O_2 in Ar, at a temperature of approximately 400°C. Future experiments are expected to yield pure VO_2 films by the careful selection of the several sputtering parameters.

F. J. Bachner

D. BONDING AND ASSEMBLY

1. Parylene

One of the methods for conformal coating of semiconductor devices is the Union Carbide licensed parylene process. The process consists essentially of three steps:

(a) Vaporization of the dimer (a white stable crystalline solid).
(b) Pyrolysis of the vapors.
(c) Deposition of the polymerized material on the surfaces to be protected.

These processes are performed in a vacuum of about 0.1 torr. We are interested in the method because the coatings are very conformal, pinhole free, and form an effective moisture and gas barrier. Also, the film has good dielectric properties and is resistant to attack by most solvents and chemicals. One of the most important criteria for deposition control and efficiency is the measurement of the percent of the dimer which is carried over and is seen as polymer on the substrate. This percentage is determined by an analysis of the dimer absorption band on an infrared spectrograph in the 14 to 14.2-μm region. Our processing is carefully controlled and our parylene films show a maximum of 1 or 2 percent dimer with some absorption bands so shallow that measurement is very difficult.

2. Optoelectronic Sensor

This package was constructed for use by Group 52 in a liquid helium dewar and has a 240-mil opening under the semiconductor chip. A 28-lead flat pack with a round cavity was selected for modification after a survey of available packages. The gold-plating of the lead frame and bonding pads of this package were then copper plated to protect these surfaces during the machining of the hole. This machining was done by the EDM spark discharge method, after which the copper plating was chromic-acid stripped, exposing the clean gold surfaces for bonding.

Installing the semiconductor chip over the package opening and subsequent bonding to the device pads requires special fixturing.

3.   Electron Beam Semiconductors

A new procedure for chip attachment, which lowers the temperature of attachment by 30°C and still maintains the low thermal resistance achieved by the earlier method of assembly, has been successfully implemented.   Higher yields result from the present technique because the problem of chip cracking is reduced considerably.   The bonding of the inner and outer shield edges presents problems because of the difficulties of alignment and visual observation during the wobble bonding operation.

4.   Environmental Testing

The 3-MHz-limiter hybrid circuit was designed by Group 63 to be temperature stable.   A test is in progress to examine the capability of the prototype hybrid units produced.   Five of these circuits are cycled, on a continuous basis, for 18 hours at 150°C followed by 8 hours at −55°C. The output varies, only not more than 10 percent, from one cycle to the next.   Samples of this circuit were satisfactorily centrifuged at 12,000 g's.   Some other samples which were spun to destruction are being carefully examined and analyzed.

<div align="right">T. F. Clough</div>

DOCUMENT CONTROL DATA – R&D

(Security classification of title, body of abstract and indexing annotation must be entered when the overall report is classified)

1. ORIGINATING ACTIVITY *(Corporate author)*	2a. REPORT SECURITY CLASSIFICATION
Lincoln Laboratory, M.I.T.	Unclassified
	2b. GROUP — None

3. REPORT TITLE

Solid State Research

4. DESCRIPTIVE NOTES *(Type of report and inclusive dates)*

Quarterly Technical Summary — 1 February through 30 April 1972

5. AUTHOR(S) *(Last name, first name, initial)*

McWhorter, Alan L.

6. REPORT DATE	7a. TOTAL NO. OF PAGES	7b. NO. OF REFS
15 May 1972	76	47

8a. CONTRACT OR GRANT NO. F19628-70-C-0230	9a. ORIGINATOR'S REPORT NUMBER(S)
b. PROJECT NO. 649L	Solid State Research (1972:2)
c.	9b. OTHER REPORT NO(S) *(Any other numbers that may be assigned this report)*
d.	ESD-TR-72-109

10. AVAILABILITY/LIMITATION NOTICES

Approved for public release; distribution unlimited.

11. SUPPLEMENTARY NOTES	12. SPONSORING MILITARY ACTIVITY
None	Air Force Systems Command, USAF

13. ABSTRACT

This report covers in detail the solid state research work of the Solid State Division at Lincoln Laboratory for the period 1 February through 30 April 1972. The topics covered are Solid State Device Research, Quantum Electronics, Materials Research, Physics of Solids and Microelectronics. The Microsound work is sponsored by ABMDA and is reported under that program.

14. KEY WORDS

solid state devices	soft x-ray	laser spectroscopy
quantum electronics	photodiodes	semiconductors
materials research	lasers	rare-earth phosphors
physics of solids	crystal chemistry	optoelectronics
microelectronics		

57